IMAGE-GUIDED HYPOFRACTIONATED STEREOTACTIC RADIOSURGERY

A Practical Approach to Guide Treatment of Brain and Spine Tumors

SECOND EDITION

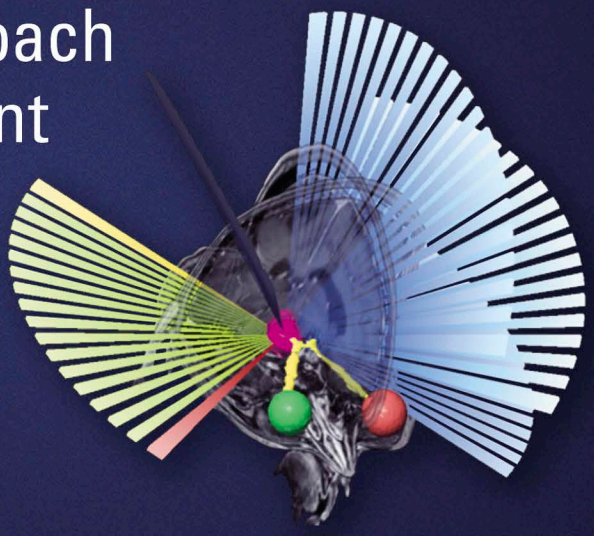

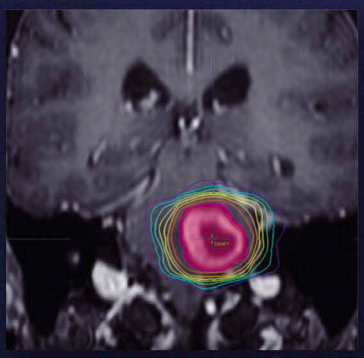

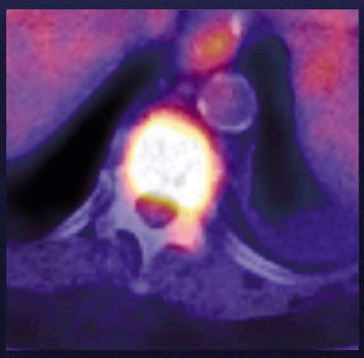

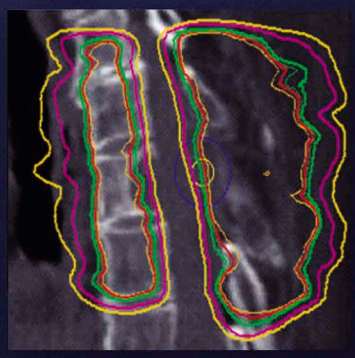

edited by

Arjun Sahgal, MD | Simon S. Lo, MD

Lijun Ma, PhD | Jason P. Sheehan, MD

CRC Press
Taylor & Francis Group

IMAGE-GUIDED HYPOFRACTIONATED STEREOTACTIC RADIOSURGERY

IMAGE-GUIDED HYPOFRACTIONATED STEREOTACTIC RADIOSURGERY

A Practical Approach to Guide Treatment of Brain and Spine Tumors

SECOND EDITION

edited by
Arjun Sahgal, MD
Simon S. Lo, MD
Lijun Ma, PhD
Jason P. Sheehan, MD

CRC Press
Taylor & Francis Group
Boca Raton London New York

CRC Press is an imprint of the
Taylor & Francis Group, an **informa** business

Second edition published 2022
by CRC Press
6000 Broken Sound Parkway NW, Suite 300, Boca Raton, FL 33487–2742

and by CRC Press
2 Park Square, Milton Park, Abingdon, Oxon, OX14 4RN

First edition published by CRC Press 2016

CRC Press is an imprint of Taylor & Francis Group, LLC

ISBN: 9780367462789 (hbk)
ISBN: 9780367478728 (pbk)
ISBN: 9781003037095 (ebk)

Typeset in Garamond Pro
by Apex CoVantage, LLC

Contents

Contributors

Ahmed Abugharib, MD
Clinical Oncology Department
Sohag University Hospital
Sohag University
Sohag, Egypt

Justus Adamson, PhD
Duke University
Department of Radiation Oncology
Durham, North Carolina

John R. Adler, MD
Zap Surgical Inc.
San Carlos, California

Christopher Alvarez-Breckenridge, MD PhD
Department of Radiation Oncology
The University of Texas MD Anderson Cancer Center
Houston, Texas

Carey Anders, MD
Department of Radiation Oncology
Duke University
Durham, North Carolina

Lilyana Angelov, MD
Department of Neurosurgery and
Rose Ella Burkhardt Brain Tumor and Neuro-Oncology Center
Cleveland Clinic
Cleveland, Ohio

Josue Avecillas-Chasin, MD
Department of Radiation Oncology
The University of Texas MD Anderson Cancer Center
Houston, Texas

Steven Babic, PhD
Department of Medical Physics
Odette Cancer Centre
Sunnybrook Health Sciences Centre
Toronto, Ontario, Canada

Ehsan H. Balagamwala, MD
Department of Radiation Oncology
Taussig Cancer Institute
Cleveland Clinic
Cleveland, Ohio

Gene H. Barnett, MD
Department of Radiation Oncology
The University of Texas MD Anderson Cancer Center
Houston, Texas

Kathryn Beal, MD
Department of Radiation Oncology
Memorial Sloan Kettering Cancer Center
New York, New York

A.M. Bergman, MD
Department of Electrical Engineering and Computer Science
Lassonde School of Engineering York University
Toronto, Ontario, Canada

John M. Boyle, MD
Department of Radiation Oncology
Duke University
Durham, North Carolina

Paul D. Brown, MD
Department of Radiation Oncology
The University of Texas MD Anderson Cancer Center
Houston, Texas

Adomas Bunevicius, MD
Department of Neurological Surgery
University of Virginia
Charlottesville, Virginia

Aimee Chan, MS
Department of Medical Imaging
Toronto, Ontario, Canada

Michael Chan, MD
University of Toronto
Hospital for Sick Children
Toronto, Ontario, Canada

Eric L. Chang, MD
Department of Radiation Oncology
Keck School of Medicine and
Norris Cancer Center
University of Southern California
Los Angeles, California

Joe H. Chang, MD
Radiation Oncology Centre
Peter MacCallum Cancer Centre
Melbourne, Australia

Samuel T. Chao, MD
Department of Radiation Oncology
Taussig Cancer Institute
and
Rose Ella Burkhardt Brain Tumor and Neuro-Oncology Center
Cleveland Clinic
Cleveland, Ohio

Steven J. Chmura, MD, PhD
Department of Radiation and Cellular Oncology
The University of Chicago
Chicago, Illinois

Cynthia Chuang, MD
Department of Radiation Oncology
Stanford University
Stanford, California

Jeffrey M. Clarke, MD
Department of Radiation Oncology
Duke University
Durham, North Carolina

Gregory J. Czarnota, PhD, MD
Department of Radiation Oncology and
Imaging Research and Physical Sciences
Sunnybrook Health Sciences Centre
and
Department of Medical Biophysics
University of Toronto
Toronto, Ontario, Canada

Sunit Das, MD
St. Michael's Hospital
University of Toronto
Toronto, Ontario, Canada

Elizabeth David, MD, FRCPC
Interventional Radiology
Sunnybrook Health Sciences Centre
University of Toronto
Toronto, Ontario, Canada

N. Dea, MD
Department of Electrical Engineering and
Computer Science
Lassonde School of Engineering York University
Toronto, Ontario, Canada

Martina Descovich, PhD
Department of Radiation Oncology
University of California, San Francisco
San Francisco, California

Jay Detsky, MD
Department of Radiation Oncology
Odette Cancer Centre
Sunnybrook Health Sciences Centre
University of Toronto
Toronto, Ontario, Canada

Kevin Diao, MD
Departments of Neurological Surgery and
Radiation Oncology
University of Pittsburgh Medical Center
Pittsburgh, Pennsylvania

Emma M. Dunne, MD
Department of Radiation Oncology
BC Cancer, Vancouver Centre
Vancouver, British Columbia

Susannah Ellsworth, MD
Department of Radiation Oncology
UPMC Hillman Cancer Center
Pittsburgh, Pennsylvania

Peter E. Fecci, MD
Department of Radiation Oncology
Duke University
Durham, North Carolina

Joel Finkelstein, MD
Sunnybrook Health Sciences Centre
University of Toronto
Toronto, Ontario, Canada

John C. Flickinger, MD
Departments of Neurological Surgery and Radiation Oncology
University of Pittsburgh Medical Center
Pittsburgh, Pennsylvania

Scott R. Floyd, MD
Department of Radiation Oncology
Duke University
Durham, North Carolina

Matthew Foote, MD
Department of Radiation Oncology
Princess Alexandra Hospital and University of Queensland
Woolloongabba, Queensland, Australia

Peter C. Gerszten, MD, MPH
Departments of Neurological Surgery and Radiation Oncology
University of Pittsburgh Medical Center
Pittsburgh, Pennsylvania

Amol J. Ghia, MD
Departments of Neurological Surgery and Radiation Oncology
University of Pittsburgh Medical Center
Pittsburgh, Pennsylvania

Stefan Glatz, MD
Department of Radiation Oncology
University Hospital Zurich
Zurich, Switzerland

Matthias Guckenberger, MD
Department of Radiation Oncology
University Hospital Zurich
Zurich, Switzerland

Michael Hardisty, MD
Sunnybrook Research Institute
University of Toronto
Toronto, Ontario, Canada

Sara Hardy, MD
Department of Radiation Oncology
University of Rochester School of Medicine
Rochester, New York

Yaser Hasan, MD
Department of Radiation Oncology
The University of Texas MD Anderson Cancer Center
Houston, Texas

Ahmed Hashmi, MD
Department of Radiation Oncology
Odette Cancer Centre
Sunnybrook Health Sciences Centre
University of Toronto
Toronto, Ontario, Canada

Chris Heyn, MD
Medical Imaging Department
Sunnybrook Health Science Centre
Toronto University
Toronto, Ontario, Canada

Zhibin Huang, PhD
Department of Radiation Oncology
East Carolina University
Greenville, North Carolina

Zain A. Husain, MD
Radiation Oncology Department
Sunnybrook Health Science Centre
Toronto University
Toronto, Ontario, Canada

Seyed Ali Jalalifar, MSc, MD
Department of Electrical Engineering and Computer Science
Lassonde School of Engineering York University
Toronto, Ontario, Canada

Einsley-Marie Janowski, MD
Department of Radiation Oncology
University of Virginia
Charlottesville, Virginia

Jonathan P.S. Knisely, MD
Department of Neurological Surgery
Weill Cornell Brain and Spine Center
New York, New York

R. Kosztyla, MD
Department of Electrical Engineering and Computer Science
Lassonde School of Engineering York University
Toronto, Ontario, Canada

Robert Koucheki, MD
Interventional Radiology
Sunnybrook Health Sciences Centre
University of Toronto
Toronto, Ontario, Canada

Jeremie Larouche, MD
Orthopedic Division
Surgery Department
Sunnybrook Health Science Centre
Toronto University
Toronto, Ontario, Canada

David Larson, MD
Department of Radiation Oncology
University of California, San Francisco
San Francisco, California

Young Lee, PhD
Department of Medical Physics
Odette Cancer Centre
Sunnybrook Health Sciences Centre
Toronto, Ontario, Canada

Eric J. Lehrer, MD
Department of Radiation Oncology
Icahn School of Medicine at Mount Sinai
New York, New York

Paula Alcaide Leon, MD
University of Toronto
Hospital for Sick Children
Toronto, Ontario, Canada

Nir Lipsman, MD
Department of Radiation Oncology
The University of Texas MD Anderson Cancer Center
Houston, Texas

M. Liu, MD
Department of Electrical Engineering and Computer Science
Lassonde School of Engineering York University
Toronto, Ontario, Canada

Simon S. Lo, MD
Department of Radiation Oncology
University of Washington
Seattle, Washington

Melissa LoPresti, MD, MPH
Department of Radiation Oncology
The University of Texas MD Anderson Cancer Center
Houston, Texas

Lijun Ma, PhD
Department of Radiation Oncology
University of California, San Francisco
San Francisco, California

Sean S. Mahase, MD
Weill Cornell Brain and Spine Center
Department of Neurological Surgery
New York, New York

Pejman Maralani, MD
Medical Imaging Department
Sunnybrook Health Science Centre
Toronto University
Toronto, Ontario, Canada

Ariel E. Marciscano, MD
Department of Radiation Oncology and Molecular Radiation Sciences
Johns Hopkins University
Baltimore, Maryland

Kajsa Mayo, BS, MD
Department of Radiation Oncology
University of Rochester School of Medicine
Rochester, New York

Nina A. Mayr, MD
Department of Radiation Oncology
University of Washington
Seattle, Washington

Mary Frances McAleer, MD, PhD
Department of Radiation Oncology
The University of Texas MD Anderson Cancer Center
Houston, Texas

Christopher McGuinness, PhD
Department of Radiation Oncology
University of California, San Francisco
San Francisco, California

John T. McKenna, MD
Weill Cornell Brain and Spine Center
Department of Neurological Surgery
New York, New York

Pejman Jabehdar Maralani, MD, FRCPC
University of Toronto
Toronto, Ontario, Canada

Hatef Mehrabian, MD
University of Toronto
Toronto, Ontario, Canada

Harley Meirovich, MD
Interventional Radiology
Sunnybrook Health Sciences Centre
University of Toronto
Toronto, Ontario, Canada

Ying Meng, MD
Department of Radiation Oncology
The University of Texas MD Anderson Cancer Center
Houston, Texas

Michael T. Milano, MD, PhD
Department of Radiation Oncology
University of Rochester School of Medicine
Rochester, New York

Michael J. Moravan, MD
Department of Radiation Oncology
Duke University
Durham, North Carolina

Hima Bindu Musunuru, MD
Departments of Neurological Surgery and
Radiation Oncology
University of Pittsburgh Medical Center
Pittsburgh, Pennsylvania

Sten Myrehaug, MD
Department of Radiation Oncology
Princess Margaret Hospital
University of Toronto
Toronto, Ontario, Canada

Mihir Naik, MD
Department of Radiation Oncology
Maroone Cancer Center, Cleveland Clinic Florida
Weston, Florida

Timothy K. Nguyen, MD
London Health Sciences Centre
Western University
London, Ontario, Canada

Alan Nichol, MD
BC Cancer Agency
Vancouver, British Columbia

Kevin Oh, MD
Department of Radiation Oncology
Massachusetts General Hospital
Boston, Massachusetts

Susan C. Pannullo, MD
Department of Neurological Surgery
Weill Cornell Brain and Spine Center
New York, New York

Phillip M. Pifer, MD
Departments of Neurological Surgery and
Radiation Oncology
University of Pittsburgh Medical Center
Pittsburgh, Pennsylvania

Luke Pike, MD
Department of Radiation Oncology
Memorial Sloan Kettering Cancer Center
New York, New York

Christopher B. Pople, MD
Department of Radiation Oncology
The University of Texas MD Anderson Cancer Center
Houston, Texas

Richard Popple, PhD
Department of Radiation Oncology
University of Alabama at Birmingham
Birmingham, Alabama

Kristin J. Redmond, MD, MPH
Department of Radiation Oncology
and Molecular Radiation Sciences
Johns Hopkins University
Baltimore, Maryland

Johannes Roesch, PhD
Department of Radiation Oncology
University Hospital Zurich
Zurich, Switzerland

Diana A. Roth O'Brien, MD
Clinical Oncology Department
Sohag University Hospital
Sohag University
Sohag, Egypt

Mark Ruschin, MD
Radiation Oncology Department
Sunnybrook Health Science Centre
Toronto University
Toronto, Ontario, Canada

Ali Sadeghi-Naini, PhD
Department of Electrical Engineering and Computer Science
Lassonde School of Engineering
York University
Toronto, Ontario, Canada

David Schlesinger, PhD
Departments of Radiation Oncology and Neurological Surgery
University of Virginia Health System
Charlottesville, Virginia

Deepa Sharma, PhD
Department of Radiation Oncology
Sunnybrook Health Sciences Centre
University of Toronto
Toronto, Ontario, Canada

Jason Sheehan, MD, PhD
Department of Neurological Surgery
University of Virginia
Charlottesville, Virginia

Hany Soliman, MD
Department of Radiation Oncology
Odette Cancer Centre
Sunnybrook Health Sciences Centre
University of Toronto
Toronto, Ontario, Canada

Gregory C. Stachelek, MD
Department of Radiation Oncology and Molecular Radiation Sciences
Johns Hopkins University
Baltimore, Maryland

John H. Suh, MD
Department of Radiation Oncology
Taussig Cancer Institute
and
Rose Ella Burkhardt Brain Tumor and Neuro-Oncology Center
Cleveland Clinic
Cleveland, Ohio

Suganth Suppiah, MD
Department of Radiation Oncology
The University of Texas MD Anderson Cancer Center
Houston, Texas

Claudio Tatsui, MD
Department of Radiation Oncology
The University of Texas MD Anderson Cancer Center
Houston, Texas

Bin S. Teh, MD
Department of Radiation Oncology
Houston Methodist Hospital
Weill Cornell Medical College
Houston, Texas

Isabelle Thibault, MD
Departement of Radiation Oncology
Centre Hospitalier Universitaire (CHU) de Québec
Université Laval
Québec, Canada

Jordan A. Torok, MD
Department of Radiation Oncology
Duke University
Durham, North Carolina

Daniel M. Trifiletti, MD
Department of Radiation Oncology
Mayo Clinic
Jacksonville, Florida

Chia-Lin Tseng, MD
Department of Radiation Oncology
Odette Cancer Centre
Sunnybrook Health Sciences Centre
University of Toronto
Toronto, Ontario, Canada

Arjun Sahgal, MD
Department of Radiation Oncology
Odette Cancer Center
Sunnybrook Hospital
Toronto, Ontario, Canada

April K.S. Salama, MD
Department of Radiation Oncology
Duke University
Durham, North Carolina

Joseph K. Salama, MD
Department of Radiation Oncology
Duke University
Durham, North Carolina

Arman Sarfehnia, MD
Radiation Oncology Department
Sunnybrook Health Science Centre
Toronto University
Toronto, Ontario, Canada

Kenneth Y. Usuki, MD
Department of Radiation Oncology
University of Rochester School of Medicine
Rochester, New York

Balamurugan Vellayappan, MD
Department of Radiation Oncology
National University Cancer Institute Singapore
Singapore

Horia Vulpe, MD
Clinical Oncology Department
Sohag University Hospital
Sohag University
Sohag, Egypt

Tony J.C. Wang, MD
Clinical Oncology Department
Sohag University Hospital
Sohag University
Sohag, Egypt

George Weidlich, MD
Zap Surgical Inc.
San Carlos, California

Shun Wong, MD
Division of Radiation Oncology
Tokyo Metropolitan Cancer and Infectious Diseases Center
Komagome Hospital
Tokyo, Japan

Victor Yang, MD
Neurosurgery Division
Sunnybrook Health Science Centre
Toronto University
Toronto, Ontario, Canada

William T. Yuh, MD
Department of Radiology
University of Washington
Seattle, Washington

K. Liang Zeng, MD
Radiation Oncology Department
Sunnybrook Health Science Centre
Toronto University
Toronto, Ontario, Canada

1 Tumor Vascular Modulation: Role of Endothelial Cells, Ceramide, and Vascular Targeted Therapies

Deepa Sharma and Gregory J. Czarnota

Contents

1.1 INTRODUCTION

At present, treating extracranial tumors with stereotactic body radiation therapy (SBRT) delivered in a single high dose or a small number of fractions is considered a standard form of treatment. Initially, this type of radiation delivery was only feasible for treating cranial tumors using stereotactic radiosurgery (SRS). Initially, SRS was used to treat arteriovenous malformations (AVMs) which are an abnormality in the brain caused by poorly formed blood vessels. Brain AVMs are known to cause major dysfunction between arteries and veins and often require medical management. Studies suggest that SRS can obliterate 50% to 90% of AVMs depending on its volume, location, and the prescribed radiation dose [1–4]. After the successful implication of SRS for treating AVMs, this technique is now being used for the treatment of brain tumors and metastases.

Recent advancements in radiation therapy with image guidance and treatment planning have made treating cranial and extracranial tumors easier with SRS and SBRT, respectively. Several preclinical and clinical studies have had a high rate of success using these techniques to treat a variety of tumors [5–8]. Classical deoxyribonucleic acid (DNA)-damage response is recognized as one of the well-known effects of radiation therapy [9][10]. However, it has since been recognized that radiation delivered at a high dose in addition initiates a signaling cascade that generates a pro-apoptotic sphingolipid known as ceramide. The biosynthesis of ceramide starts with the hydrolysis of sphingomyelin by acidic sphingomyelinase (ASMase) on the outer leaflet of endothelial cell membranes. The clustering and aggregation of ceramide molecules on the cell membrane stimulate endothelial cell apoptosis. The addition of ASMase and/or ceramide inhibitors halts this entire process. These phenomena have been reported in numerous xenograft models including fibrosarcoma and melanoma transplanted in wild-type and ASMase knockout mice and are now established as predictive of a preclinical response [8]. The role of ceramide endothelial cell apoptosis has been elusive in clinical studies with few studies suggesting ceramide as a marker to distinguish between responding and non-responding patients. A study by Satiskumar

et al. demonstrated that substantial increases in serum secretory sphingomyelinase (S-SMase) activity and ceramide levels in patients treated with a single high dose of 15 Gy were correlated with good clinical outcomes. Conversely, non-responding patients did not exhibit any increment in serum S-SMase and ceramide [11]. Similarly, patients with liver and lung oligometastases of colorectal cancer origin exhibited significant elevation in plasma ceramide levels subsequently resulting in reduced tumor volume. In contrast, the non-responding patients exhibited a drop in plasma ceramide and an increase in tumor volume [12].

The preclinical and clinical experiences with SRS/SBRT show remarkable outcomes. However, the biological mechanisms leading to these outcomes are not fully understood. High-dose radiotherapy can destroy tumor vasculature as a result of gross endothelial cell apoptosis that leads to additional indirect/secondary tumor cell death [8, 13]. Such indirect tumor cell death can further enhance an anticancer immune response, which is activated by the release of tumor antigens from dying tumor cells [14–17]. Thus, due to the enhanced cell kill and antitumor effects observed following SRS and SBRT, there has been a paradigm shift in standard radiobiological understanding.

1.2 CHALLENGES IN RADIOBIOLOGICAL MODELING FOLLOWING HIGH RADIATION DOSES

In 1975, Rodney Withers introduced four factors that determine the response to fractionated radiotherapy known as the 4R's of radiobiology: repair, repopulation, redistribution, and reoxygenation [18]. The 4R's of radiobiology can link to the success or failure of conventional fractionated radiation therapy. However, the model becomes ineffective when tumors are treated at high doses with SRS or SBRT. ***Repair:*** At higher doses, the repair of sublethal DNA damage rates reduces due to the saturation of repair mechanisms [19]. Also, a higher radiation dose delivered over a short duration can lead to increased DNA damage which might cause more complicated alterations making it difficult to repair [20]. ***Repopulation:*** SRS and SBRT treatments are typically given over the course of a week. The repopulation of tumor cells is almost impossible during this short time. ***Redistribution:*** When cells are exposed to extremely high doses (e.g., 20 Gy), cell cycle progression is interrupted resulting in an immediate cell cycle arrest. This causes the cells to die at the cell cycle phase they were in at the time of irradiation. This is different from when cells are treated with a low dose that causes the cells to preferentially die at G2/M-phase [21]. ***Reoxygenation:*** A radiation dose higher than 10 Gy per fraction causes severe vascular damage which can elevate the hypoxia level in the intratumoral microenvironment and halt the reoxygenation process for hypoxic cells due to the short overall treatment time of single-dose radiotherapy. With each fraction of conventional fractionated radiation therapy, the death of oxic tumor cells at the tumor periphery allows the reoxygenation of hypoxic cells deeper within the tumor, restoring radiosensitivity, unlike radiation delivered at high doses, which causes both oxic and hypoxic cells to undergo secondary cell death [22]. Thus, the 4R's of radiobiology are generally ineffective at modelling the response to the high doses of radiation given with SRS and SBRT. Another radiobiological model was introduced in 1989 by Fowler known as the linear-quadratic model (LQ model), which estimates the prediction of tumor survival in response to varying radiation doses [23]. It is reported that the LQ model can accurately predict cell kill resulting from DNA damage at conventionally fractionated doses. However, the model may overestimate cell kill at high doses due to the occurrence of both direct and indirect cell deaths [24]. The tumor cell survival curve based on the LQ model depicts a sharp bend in the curve in response to increasing radiation doses because of the additional tumor cell death that appears only at doses higher than 10 Gy. The LQ model is generated largely based on in vitro data that incorporates doses lower than what is used in SRS/SBRT making its utility inappropriate at high doses per fraction [25]. Therefore, while the 4R's and the LQ model of radiobiology can easily be implemented to estimate the response of conventional fractionated radiation therapy, the use of these principles for predicting the outcome of SRS and SBRT remains up for debate.

1.3 RADIOBIOLOGICAL DETERMINANTS OF HIGH-DOSE RADIOTHERAPY

The progression and metastases of cancer depend on the homeostasis of the tumor microenvironment, which comprises different cell populations [26, 27]. It is evident that cancer treatments, including

chemotherapy and radiation therapy, target not only the tumor but also other cellular components like vascular endothelial cells and immune cells. The surge in interest in the contribution of endothelial cells to the tumor response began in 1971 when Judah Folkman first recognized that the growth and survival of tumors depend on angiogenesis [28, 29]. The process of angiogenesis relies on the proliferation, migration, and remodeling of endothelial cells [30, 31]. Endothelial cells are known to be the primary target for radiation-induced cell death because they are enriched (20-fold as compared to other cells) in secretory ASMase [32]. An increase in ASMase-induced ceramide generation is mandatory to achieve the endothelial apoptotic effect [8, 13, 33, 34].

A study by Garcia-Barros *et al*. demonstrated that endothelial cell apoptosis occurs as a primary event and is followed by secondary tumor cell death, which contributes to the overall radiation-induced tumor response. Experiments conducted with mice deficient in ASMase and Bcl-2-associated X protein (Bax), implanted with MCA/129 fibrosarcomas and B16F1 melanoma tumors, resulted in enhanced tumor growth by 200% to 400% compared to their wild-type counterparts. Wild-type (ASMase+/+) mice exhibited a significant increase in endothelial cell death within 1 to 6 hours following a dose of 15–20 Gy, while the tumor cells in the same mice remained intact for 2 to 3 days. The occurrence of tumor cell death days later, subsequently, led to increased tumor growth delay and overall tumor cure by 50% [8]. The mechanism regulating the endothelial cell apoptosis that contributes to the overall tumor response is known to be dependent on the activation of the ASMase–ceramide pathway. Within a few hours of irradiation, the accumulation of ceramide in the endothelial compartment causes its rapid destruction followed by an avalanche of tumor cell death. A study conducted by Santana *et al*. reported that lymphoblasts from Niemann–Pick patients who are ASMase-deficient abrogated the process of radiation-induced ceramide formation and apoptosis. A retroviral transfer of human ASMase cDNA reversed this phenomenon by inducing ceramide-dependent apoptosis. Furthermore, exposure of fibrosarcoma-bearing wild-type (ASMase+/+) mice to 20 Gy in a single dose demonstrated significant apoptotic cell death in the lung and thymic tissue. In (ASMase−/−) mice, the same radiation dose failed to induce ceramide generation and apoptosis in endothelial cells [34]. Pena and colleagues reached a similar conclusion demonstrating significant endothelial cell apoptosis in a dose- and time-dependent manner following irradiation of the central nervous system (CNS) of C57BL/6 mice with a dose of 5 to 100 Gy. It was found that endothelial cell death accounted for up to 20% of radiation-induced apoptosis in CNS specimens, peaking at 12 hours within a window of 4 to 24 hours after irradiation. Intravenous injection of fibroblast growth factor (FGF) and basic endothelial growth factor (bFGF), before and after giving the dose of 50 Gy, inhibited endothelial cell apoptosis [35]. Thus, these studies suggest that endothelial cell death happening after a high dose is primarily responsible for overall tumor response mediated by the ASMase–ceramide pathway. Some studies contradict these findings and emphasize that tumor cells are responsible for enhanced radiation response.

To determine the role of tumor cells in the radiation response, severe combined immunodeficiency (SCID) mice deficient in the DNA double-strand break repair gene DNA-dependent protein kinase (DNA-PKcs−/−) were inserted with a functional (DNA-PKcs+/+) gene. Exposure to a single dose of 30 Gy or 4 × 5 Gy fractions delivered over 2 days resulted in a substantial tumor growth delay of 1.5-fold in (DNA-PKcs−/−) mice compared to their (DNA-PKcs+/+) counterparts. Thus, the inoculation of the functional DNA repair gene into tumor cells restored radioresistance resulting in a reduced radiation response [36]. Furthermore, Moding and colleagues incorporated a dual recombinase technology to generate primary sarcomas in genetically engineered mouse models with targeted mutations in both endothelial cells and tumor cells. The study showed that primary sarcoma with Bax, a pro-apoptotic gene, and ataxia telangiectasia mutated (Atm), a DNA damage response gene, removed from mouse endothelial cells and tumor cells exhibited different outcomes. The removal of the Bax and Atm gene from mouse endothelial cells did not impact the primary sarcoma response to radiation therapy of 20 Gy. On the contrary, the same genes removed from mouse tumor cells resulted in a significant increase in tumor cell death and growth inhibition of primary sarcoma. Thus, the study revealed that tumor cells, but not endothelial cells, are the prime determinants of radiation response [37]. An interesting observation from Ogawa *et al*. indicated that tumor cells in nude mice are crucial for determining radiation response, whereas in SCID mice, damage to both tumor cells and endothelial cells governs the radiosensitivity [38].

After a controversial debate of whether or not endothelial cells determine tumor response to radiation therapy, Garcia-Barros *et al*. conducted experiments with SCID mice, a model known to carry a germline mutation in their DNA repair gene [39]. These mice are also 2.5- to 3.0-fold more radiosensitive compared to other mouse models [40–42]. To confirm the engagement of the endothelial component in radiation responses, MCA/129 fibrosarcomas and B16 melanomas grown in SCID (ASMase+/+) and C57BL/6 (ASMase+/+) mice were exposed to high-dose radiotherapy. A single dose of 20 Gy resulted in a significant endothelial cell death in both SCID (ASMase+/+) as well as C57BL/6 (ASMase+/+) mice. The tumor growth delay in SCID (ASMase+/+) mice occurred in a pattern similar to wild-type C57BL/6 (ASMase+/+) mice. Endothelial apoptosis and tumor growth were abrogated in tumors implanted in (ASMase−/−) mice. Thus, the study concluded that the endothelial compartment is solely responsible for enhanced radiation response and that the tumor cells do not impact the radiation-induced endothelial cell apoptosis and overall radiation response [5].

1.4 CELLULAR RESPONSE TO HIGH-DOSE RADIATION THERAPY

1.4.1 DIRECT AND INDIRECT CELL DEATH INDUCED BY HIGH-DOSE RADIATION

For many years, it was believed that cell death induced by ionizing radiation is mainly dependent on DNA damage [9, 10]. However, this belief was changed when an alternative mechanism was provided demonstrating single high doses of radiotherapy inducing plasma membrane alteration that can lead to the activation of the sphingomyelin pathway followed by ceramide generation [43, 44]. Ceramide, once formed, can serve as a second messenger, triggering various apoptotic signaling pathways. A study by Haimovitz-Friedman *et al*. confirmed the involvement of ceramide in the apoptotic response using bovine aortic endothelial cells (BAEC). The ceramide level reached its maximum within few minutes of radiation exposure (10 Gy in a single dose) in whole-cell lysates as well as in nuclei-free membranes prepared from BAEC. Thus, this study confirmed that radiation-induced apoptosis can be independent of DNA damage [33]. It is now evident that there is more than one pathway of radiation-induced cell death (Figure 1.1). Generally, a low dose of radiation induces cytotoxic effects on DNA eliciting DNA double-strand breaks, which cause direct tumor cell death [45–47]. High-dose radiation, on the other hand, can kill tumor cells directly, by causing DNA damage, or indirectly in p53-dependent manner or by causing massive tumor vasculature collapse through endothelial cell damage [8, 48, 49]. High-dose-induced vascular dysfunction can further cause tumor cell death by evoking tumor hypoxia and an immune response.

The occurrence of tumor cell death as a result of significant vascular endothelium damage following high-dose radiotherapy was first reported by Garcia-Barros and colleagues. Their results demonstrated that ASMase-deficient mice abrogated apoptosis of endothelial cells while the wild-type phenotype exhibited significant endothelial and tumor cell death. This confirmed that ASMase–ceramide activation is crucial for radiation-induced vascular endothelial damage [8]. Several other studies have also reported the involvement of ceramide-induced endothelial cell apoptosis in regulating the overall tumor response. A large body of work by Czarnota *et al*. has indicated that pre-treatment with ultrasound-stimulated microbubbles (USMB) before administering a radiation dose of 8 Gy can cause a significant elevation of ceramide leading to massive vascular endothelial cell death [50]. El Kaffas *et al*. investigated the dose-dependent effect of radiation in combination with USMB using MCA/129 fibrosarcoma-bearing wild-type (ASMase+/+) mice, knockout (ASMase−/−) mice, and wild-type mice treated with sphingosine-1-phosphate (S1P), a ceramide antagonist. In (ASMase+/+) mice, a combination of USMB and dose of 8 Gy resulted in the highest level of cell death of 8.7% at 3 hours, 53.2% at 24 hours, and 37.8% at 72 hours compared to radiation (8 Gy) only, which resulted in 10.0%, 17.3%, and 15.4% cell death at 3, 24, and 72 hours, respectively. Furthermore, USMB combined with radiation treatment resulted in a 40% attenuation of tumor blood flow within 24 hours, which persisted to 72 hours. The shutdown of the vasculature at 24 hours was reported to be accountable for endothelial cell death. The study further indicated that the ceramide level in (ASMase+/+) mice escalated within 24 hours of administering treatment with USMB and 8 Gy of radiation treatment, which confirmed the involvement of endothelial ASMase–ceramide activation leading to overall tumor vascular disruption [51].

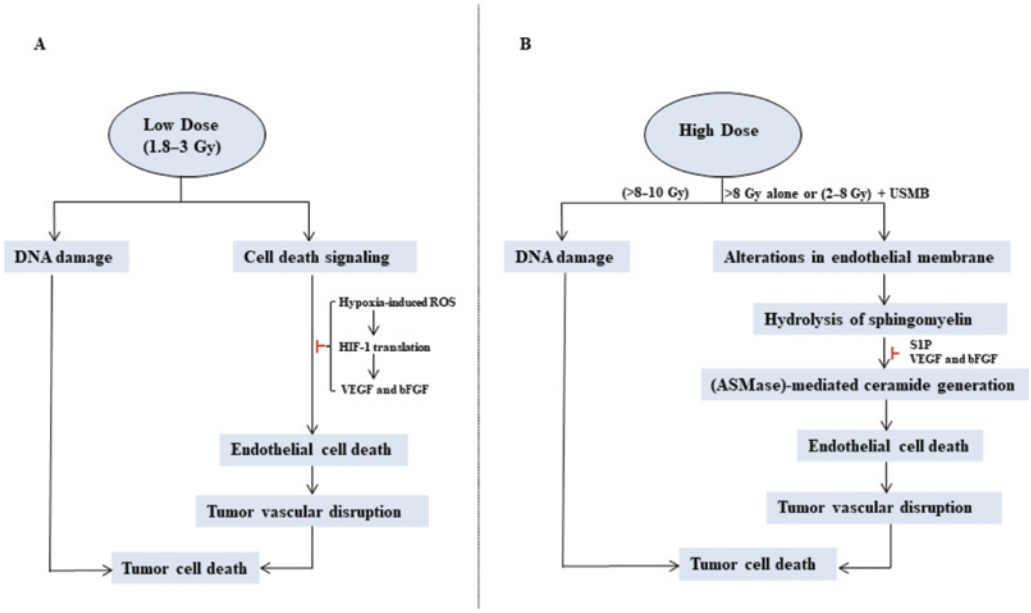

Figure 1.1 Endothelial and tumor cells' response to low- and high-dose radiotherapy.

Numerous other studies have also indicated a decrease in tumor perfusion concomitant with endothelial cell death. Irradiation of neuroblastoma xenografts following radiation (12 Gy) reduced the tumor blood volume by 63%, subsequently causing endothelial cell damage [52]. Similarly, rats bearing orthotopic human brain tumors exposed to a single dose of 20 Gy exhibited significant apoptosis and an 80% decrease in tumor blood flow within 2 hours of irradiation, suggesting that changes in vascularity correspond to endothelial damage [53].

Prior studies by Song and colleagues performed with FSaII fibrosarcoma tumors of mice demonstrated a severe decline in blood perfusion accompanied by elevated hypoxia within 1 to 5 days following a single dose of 20 Gy. The delayed secondary tumor cell death reported in this study was a ramification of extensive tumor vascular occlusion and increased intratumoral hypoxia [54]. Radiation-induced vascular damage is also known to cause hypoxic cell death. Upon exposure to a high dose, a fraction of hypoxic cells that survive the direct and indirect cell death later become devoid of nutrients, ultimately resulting in death. Also, vessels appearing nonfunctional due to reduced nutrients and oxygen resulting from massive radiation-induced tumor cell death might contribute to hypoxic cell death. It was reported that mice bearing FSaII fibrosarcoma exposed to a single dose of 20–30 Gy exhibited a decrease in cell survival by 3–4 logs, whereas a dose high up to 90 Gy was essential for the reduction of cell survival by 8 logs. The progressive cell survival loss that occurred after irradiation was caused by nutrient deprivation [55, 56]. Similar observations were reported by Hill and colleagues in a mouse KHT sarcoma model. Irradiation of tumors with a single dose of 20 Gy caused the death of hypoxic cells by a factor of 3 to 4 [57]. These data confirm the presence of hypoxic cell death in addition to tumor cell death as a result of vascular damage after high-dose radiotherapy.

In addition to the direct and indirect cell death effects, SRS and SBRT are known to trigger an antitumor immune response. Radiation-induced tumor cell death elicits the release of tumor antigens causing immunogenic cell death (ICD) [58]. Dying irradiated tumor cells release high mobility group box 1 (HMGB1) protein that interacts and activates toll-like receptor (TLR)-4 on the dendritic cells inducing an antitumor response [59]. Recently, a mathematical framework based on murine breast experimental data suggested that a radiation dose between 10 and 13 Gy per fraction is required to induce antitumor immunity [60]. Taken together, these studies suggest that SRS and SBRT are likely to kill more cancer cells

as compared to conventional fractionated radiotherapy. The direct cell death in response to DNA damage and the indirect secondary tumor cell death mediated by vascular dysfunction account for the majority of cell killing. In addition, massive hypoxic cell death due to the deterioration of the intratumor microenvironment (assuming 20% of the tumor cells are hypoxic in solid tumors) combined with the tumor cell kill caused by an enhanced antitumor immune response further contribute to the cell death following SRS and SBRT.

1.4.2 RADIATION-INDUCED VASCULAR CHANGES

Our understanding of tumor vasculature has evolved over the past several years. Unlike normal vasculature, which is arranged hierarchically with evenly distributed arteries, veins, and capillaries, tumor vasculature remains highly disorganized, irregular, chaotic, dilated, leaky, and tortuous with no ability to differentiate between arterials and venules [61]. The endothelial layers in normal blood vessels are regularly shaped and are fully supported by organized pericytes that act as a basement membrane. On the contrary, the structure of tumor blood vessels is constructed with an inner single layer of endothelial cells that are poorly connected with uneven support of abnormal pericytes [62]. Due to these morphological abnormalities, tumor blood vessels are highly vulnerable to ionizing radiation. Several studies have reported drastic vascular changes following high-dose radiation therapy. Along with changes in structural integrity, fluctuations in tumor blood flow and tumor oxygenation are probably the most notable changes reported following a radiation dose higher than 8 to 10 Gy. Radiation-induced vascular changes in multiple tumor types have been reviewed in detail by Park *et al*. Collective data from human studies suggest a general trend of a slight increase in tumor blood flow, or no change in blood flow in some cases, observed at the beginning of a fractionated radiotherapy followed by a reduction toward the end of the course of treatment [63]. For preclinical animal models, exposure to conventionally fractionated radiotherapy of dose of 1.5 to 2.0 Gy causes no changes in vasculature in the early period of radiation with a slight vascular dysfunction reported at a later phase of irradiation [64, 65]. However, a single dose of 5 to 10 Gy causes moderate vascular damage and [64–66] increasing the dose to more than 10 Gy/fraction leads to extreme tumor vasculature deterioration [54].

Radiation-induced tumor vascular effects are known to be widely dependent on radiation dose, duration between the doses, tumor type, stages, and the site of the tumor. An extensive body of work has previously been reported by Song and colleagues regarding the vascular changes in irradiated tumors using Walker 256 carcinomas grown in the hind leg of rats. Tumors exposed to a single dose of 2, 5, 10, 30, and 60 Gy were monitored several days after irradiation (intravascular volume and extravasation rates of plasma protein/vascular permeability were measured). Radiation doses of 2 and 5 Gy did not induce much of a vascular response. However, a single dose of 10, 30, or 60 Gy resulted in a significant abolishment of vascular volume after the second, sixth, and twelfth days of irradiation [64]. Several other studies have also reported tumor blood flow reduction upon high-dose delivery. They suggest that a dose higher than 10 Gy in a single fraction is more effective in causing vascular damage than the same dose given in fractions [67]. Tumors treated with a fractionated dose initiate a transient increase followed by a rapid fall in vascular volume as the number of fractions increases. This is contrary to what is observed with a single high dose which results in a sharp decline in vascular volume throughout the tumor.

Radiation-induced vascular changes are known to greatly influence tumor oxygenation, but there are conflicting reports on whether the vascular damage contributes to changes in oxygen tension or not. Tumor oxygenation monitored in rats bearing rhabdomyosarcomas following a fractionated radiotherapy treatment of 60 Gy administered in 20 fractions over a period of 4 weeks showed no significant changes in partial pressure of oxygen (pO_2) measurements until week 3. However, at week 4, a significant decrease in tumor pO_2 was reported, which was attributed to be due to the obstruction of tumor capillaries [68, 69]. On the other hand, exposing A-07 human melanoma xenografts to a single dose of 10 Gy resulted in a 40% drop in blood perfusion and 25% increase in extracellular volume fraction within 72 hours. In this case, the tumor pO_2 content remained unchanged suggesting no correlation between vascular changes and oxygenation [70]. Heterogeneity in tumor vascular perfusion and oxygenation has frequently been reported. An observed phenomenon of reduced blood volume at the center of the tumor compared to the rim has been seen in many tumor types [71]. Patients with advanced non-small-cell lung cancer administered a dose of

27 Gy in 2, 4, and 6 fractions resulted in an increased vascular blood volume at the tumor rim by 31.6%, 49.3%, and 44.6%, respectively. The blood volume in the tumor center remained 16.4%, 19.9%, and 4.0% with the same fractions of radiotherapy [72]. An important observation by Mottram suggests that tumor cells at the periphery are more radiosensitive compared to the cells in the center of the tumor. Cells localized at the periphery are closer to nearby blood vessels and, therefore, have abundant oxygen supply [73]. In 1955, Thomlinson and Gray performed a detailed quantitative examination of carcinoma of the bronchus to study the radiosensitivity of marginal and central cells within a tumor. They found that the cells close to capillaries acquired sufficient amounts of nutrients/oxygen and remained proliferative, while the cells located at a distance greater than about 100 μm from the capillaries remained non-viable. The lower oxygen content in the central region during the time of irradiation made the cells more radioresistant compared to the peripheral cells that were well-oxygenated [74, 75].

1.5 COMBINING RADIOTHERAPY AND ANTI-ANGIOGENESIS STRATEGIES

In most solid tumors, the vasculature remains highly heterogeneous. Tumor angiogenesis keeps the tumor alive by supplying essential nutrients and oxygen [29]. The balance of several angiogenic regulators is required for the growth and metastases of tumors [76]. Targeting tumor vasculature for the treatment of solid tumors has shown exceptional success over several years. Currently, various vascular targeting agents, such as anti-angiogenic agents and vascular disrupting agents, are being extensively investigated in preclinical and clinical studies [77, 78]. Several clinical trials are currently being conducted to treat cancer in humans using angiogenesis inhibitors. Some of the agents approved for clinical trials are listed in Table 1.1. Anti-angiogenic agents are known to inhibit and, in some cases, completely stop the growth of new blood vessels [78], whereas vascular disrupting agents are designed to selectively decrease or shutdown the tumor blood flow [77, 79, 80].

Tumors promote the growth of new blood vessels by secreting numerous angiogenic growth factors such as basic fibroblast growth factor (bFGF) and vascular endothelial growth factor (VEGF). Endothelial cells in pre-existing vessels express several receptors to which this angiogenic growth factor binds and initiates various signaling pathways [81, 82]. The use of angiogenesis inhibitors/agents blocks the formation of new blood vessels, preventing the growth and progression of the tumor by alleviating ASMase-generated ceramide [83]. Work by Truman *et al*. indicated that radiation-induced ceramide acts as a rheostat for the survival and death of endothelial cells and that the timing of anti-angiogenic treatment is crucial for sensitizing tumors. The study showed bFGF and VEGF inhibited radiation-induced ASMase–ceramide activation, and apoptosis was reversed by the addition of endogenous C16 ceramide in MCA/129 fibrosarcoma. Pre-treatment of tumors with DC101, an angiogenesis inhibitor, 1 hour prior to radiotherapy with 13.5 Gy led to enhanced ASMase-generated ceramide, subsequently causing endothelial cell apoptosis. However, DC101 injected 1 hour after radiation remained ineffective [84]. Similar observations were reported by Rao *et al*. indicating that VEGF inhibitor axitinib administered 1 hour prior to radiation therapy increased tumor radiosensitivity. A dose of 27 to 40 Gy in a single exposure combined with axitinib caused endothelial cell death both in vitro in primary cultured cells and in vivo in mice bearing MCA/129 sarcoma or B16F1 melanoma. A growth delay of the tumor and complete response rate by 40% was also observed in these mice followed by a combination of radiation and axitinib [85]. Tumor response following treatment with a combination of angiogenic inhibitors/agents and radiation has also been reported in several studies; however, the exact mechanism of interaction between angiogenic inhibitors and radiotherapy is still unknown. An anti-angiogenic/vascular targeting agent combined with radiation is expected to enhance tumor response by reducing tumor blood perfusion and oxygenation. However, studies indicate the occurrence of increased tumor blood flow and oxygen concentration following a combination of both [86–89]. Breast (MDA-MB-231) xenografts, when exposed to a single dose of 8 and 16 Gy combined with sunitinib, a VEGF inhibitor, demonstrated significant cell death and a subsequent increase in tumor blood flow by 50% [89]. It was attributed that a single high dose of radiation can cause damage to abnormal blood vessels, while the addition of sunitinib may allow vessel normalization causing increased oxygenation.

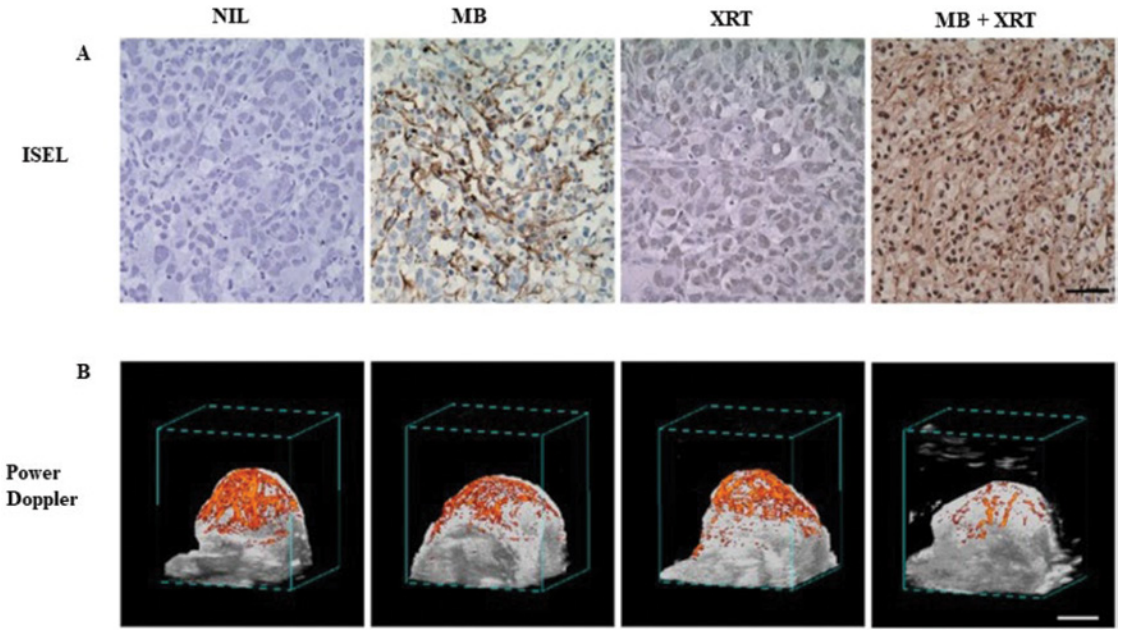

Figure 1.2 Histochemical staining of PC3 tumor xenograft endothelial cells with ISEL and power Doppler ultrasound images of PC3 tumor xenografts reveal response to treatment at 24 hours.

In recent years, USMB therapy has proven to be a novel form of targeted anti-angiogenic therapy. Microbubbles are small gas-filled bubbles ranging in size from 1 to 4 μm and are widely used as an ultrasound contrast agent due to their excellent acoustic response [90]. Upon contact with ultrasound waves, microbubbles can oscillate, expand, and collapse contributing to overall changes in the surrounding tissue environment. Disruption of the bubbles upon exposure to ultrasound acoustic pressure can cause a severe vascular disruption enhancing tumor response [91]. A large body of work by Czarnota and colleagues demonstrates that a combination of radiotherapy and USMB causes significant endothelial cell death followed by microvascular deterioration. A study performed on prostate tumor xenografts (PC3) treated with a radiation dose of either 2 or 8 Gy combined with a low or high dose of USMB treatment showed significant cell death of 44 ± 13% (mean ± standard error) with 2 Gy + USMB and 70 ± 8% with 8 Gy + USMB. Vascular disruption detected using power Doppler ultrasound indicated a decrease in tumor blood flow of 18 ± 22% (mean ± standard error) with radiation alone, 20 ± 37% with USMB alone, and 65 ± 8% with a combination of 8 Gy and USMB (Figure 1.2). Furthermore, the group receiving the combined treatment exhibited significant tumor growth delay and fewer proliferating cells [50]. Data from other mouse models bearing breast, bladder, and fibrosarcoma tumors have also revealed a similar effect using these combination therapies [51, 92–94]. The endothelial cell death-induced vascular dysfunction observed with a combination of radiation and USMB is found to be ceramide-dependent. USMB is known to cause a mechanical perturbation in the endothelial cell membrane leading to enhanced ceramide generation followed by vascular destruction. A study by Kim *et al*. reported 14-fold higher ceramide content in PC3 xenografts following treatment using a combination of USMB and radiation (8 Gy). The increased ceramide level was linked to enhanced tumor cell death and vascular damage [95]. Subsequently, Al-Mahrouki and colleagues extensively investigated the genetic pathway involved in the regulation of ceramide-mediated tumor vascular disruption following the administration of USMB and radiation therapy. In particular, they studied the role of UDP glycosyltransferase 8 (UGT8) in tumor response enhancement. UGT8 is a key enzyme that catalyzes the transfer of galactose to ceramide. Experiments were conducted with genetically modified PC3 cells and tumor xenografts generated from stably transfected PC3 cells with a downregulated UGT8 gene. A combination of USMB and dose of 8 Gy caused greater cell damage in the downregulated UGT8 tumor

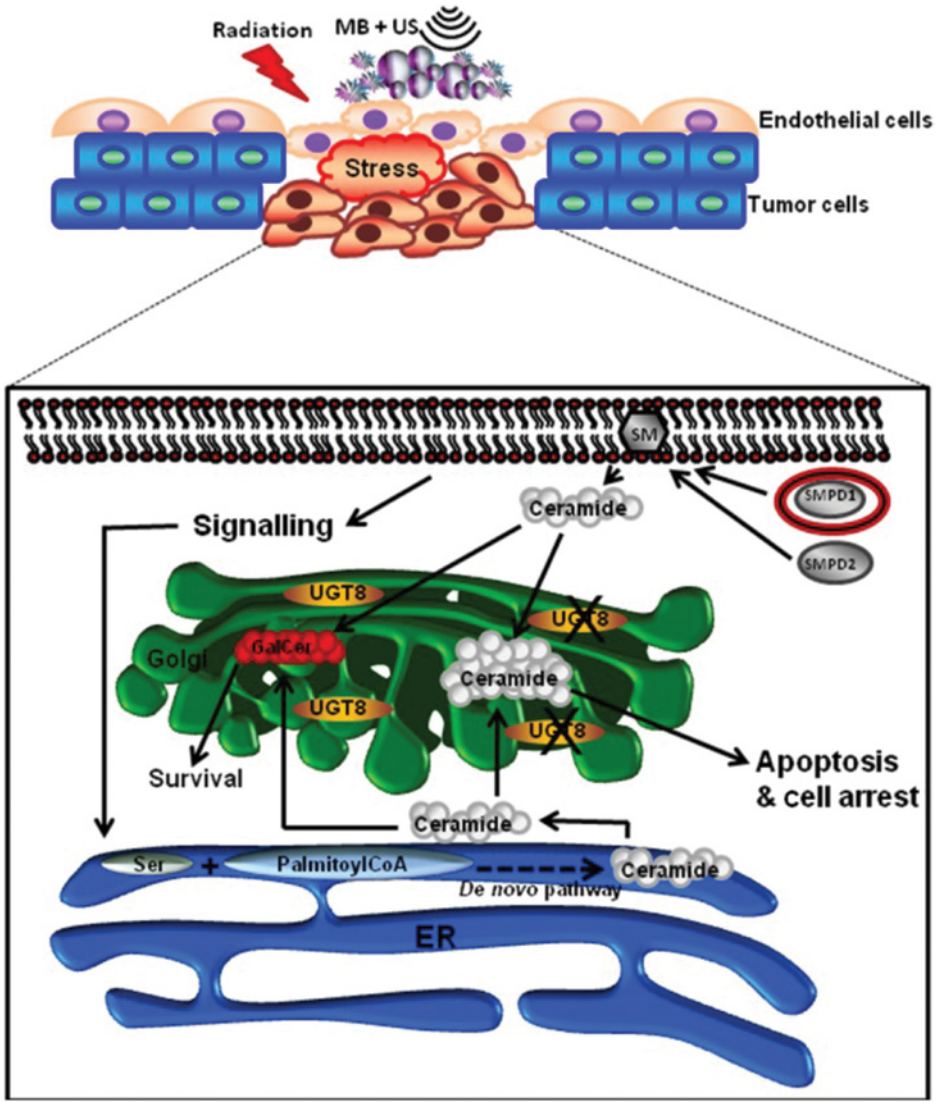

Figure 1.3 Model depicting UGT8 signaling and its role in ceramide biosynthesis.

model as compared to control tumors. In addition, they reported a significant decrease in the level of tumor blood flow and oxygen saturation in the UGT8 downregulated model. An increase in tumor response was found to be concomitant with a greater amount of ceramide accumulated due to the downregulation of the UGT8 gene (Figure 1.3) [96]. Thus, targeting UGT8 combined with vascular disrupting therapy might be a good starting point for the further exploration and optimization of this new treatment strategy for cancer.

1.6 CONCLUSION

SRS/SBRT is increasingly being recognized as one of the essential treatment options for cancer. A high radiation dose delivered in a single fraction or in a small number of fractions affects the tumor vasculature by causing ceramide-mediated endothelial apoptosis leading to indirect/secondary tumor cell death. The indirect tumor cell death further evokes an immune response resulting in an overall enhancement in radiation response. Ceramide generation by the activation of the ASMase pathway is a central determinant of

Table 1.1 **Angiogenesis inhibitors/agents undergoing clinical trials for treating human cancers**

ANGIOGENESIS INHIBITORS/AGENTS	BRAND NAME
Axitinib	Inlyta
Bevacizumab	Avastin
Cabozantinib	Cometriq
Everolimus	Afinitor
Lenalidomide	Revlimid
Lenvatinib mesylate	Lenvima
Pazopanib	Votrient
Ramucirumab	Cyramza
Regorafenib	Stivarga
Sorafenib	Nexavar
Sunitinib	Sutent
Thalidomide	Synovir, Thalomid
Vandetanib	Caprelsa
Ziv-aflibercept	Zaltrap

radiation-induced vascular endothelial cell damage. By upregulating ASMase-released ceramide using various angiogenesis inhibitors and/or anti-angiogenic therapy (USMB), tumor radiosensitivity can be restored.

Damage to endothelial cells and tumor cells appears to be instigated by both low dose (1.8–3 Gy) and single high dose (>8 Gy) alone or combined with USMB (2–8 Gy + USMB). (A) With each low-dose fraction, hypoxia-mediated ROS results in HIF-1 translation making the cells radioresistant. Inhibition of HIF-1 leads to massive endothelial cell death, microvascular damage, and increased tumor cell death. (B) High-dose-induced tumor cell death is mediated via rapid translocation of lysosomal ASMase to the extracellular leaflet of endothelial cell membranes resulting in ceramide generation. The accumulation of ceramide in endothelial cells causes its disruption followed by vascular collapse and tumor cell death. The addition of S1P, VEGF, and bFGF can halt this entire process. *Abbreviations*: ASMase, acid sphingomyelinase; bFGF, basic fibroblast growth factor; DNA, deoxyribonucleic acid; HIF-1, hypoxia-inducible factor 1; ROS, reactive oxygen species; S1P, sphingosine-1-phosphate; USMB, ultrasound-stimulated microbubbles; VEGF, vascular endothelial growth factor.

(A) Tumors treated with a combination of USMB and radiation (8 Gy dose) exhibited increased cell death confirmed with ISEL staining. ISEL-positive cells can be identified by a dark-stained nucleus. The scale bar represents 60 microns. (B) A significant drop in the blood flow signal was observed following a combination of USMB and radiation compared to control groups with no treatment or treatments including USMB only and radiation only. The scale bar represents 2 mm. Adapted from [50]. ISEL= *in situ* end-labeling; MB= microbubble; NIL= no microbubble; XRT= radiation.

The *de novo* biosynthesis of ceramide takes place in the endoplasmic reticulum. Elevated expression of UGT8 converts ceramide to galactosylceramide resulting in degradation of ceramide and inhibition in the apoptotic signaling pathway. Conversely, UGT8, when underexpressed, leads to elevated ceramide levels initiating a cell death signaling pathway [96]. ER, endoplasmic reticulum; GalCer, galactosylceramide; MB + US, microbubble + ultrasound; S1P, sphingosine-1-phosphate; Ser, serine; SM, sphingomyelin; SMPD1, sphingomyelin phosphodiesterase 1; SMPD2, sphingomyelin phosphodiesterase 2; UGT8, UDP glycosyltransferase 8.

REFERENCES

1. Ding D, Starke RM, Kano H, Mathieu D, Huang P, Kondziolka D, et al. Radiosurgery for erebral arteriovenous malformations in a randomized trial of unruptured brain arteriovenous malformations (ARUBA)-eligible patients: A multicenter study. *Stroke*. 2016;47.
2. Andrade-Souza YM, Ramani M, Scora D, Tsao MN, TerBrugge K, Schwartz ML. Radiosurgical treatment for rolandic arteriovenous malformations. *J. Neurosurg*. 2006.
3. Hanakita S, Koga T, Shin M, Igaki H, Saito N. Application of single-stage stereotactic radiosurgery for cerebral arteriovenous malformations >10 cm^3. *Stroke*. 2014.
4. Rubin BA, Brunswick A, Riina H, Kondziolka D. Advances in radiosurgery for arteriovenous malformations of the brain. *Neurosurgery*. 2014;74.
5. García-Barros M, Thin TH, Maj J, Cordon-Cardo C, Haimovitz-Friedman A, Fuks Z, et al. Impact of stromal sensitivity on radiation response of tumors implanted in SCID hosts revisited. *Cancer Res*. 2010.
6. Baumann R, Chan MKH, Pyschny F, Stera S, Malzkuhn B, Wurster S, et al. Clinical results of mean GTV dose optimized robotic-guided stereotactic body radiation therapy for lung tumors. *Front Oncol*. 2018;8.
7. Berkovic P, Gulyban A, Nguyen PV, Dechambre D, Martinive P, Jansen N, et al. Stereotactic robotic body radiotherapy for patients with unresectable hepatic oligorecurrence. *Clin Colorectal Cancer*. 2017;16.
8. Garcia-Barros M, Paris F, Cordon-Cardo C, Lyden D, Rafii S, Haimovitz-Friedman A, et al. Tumor response to radiotherapy regulated by endothelial cell apoptosis. *Science*. 2003;80.
9. Radford IR. The level of induced DNA double-strand breakage correlates with cell killing after x-irradiation. *Int J Radiat Biol*. 1985.
10. Ward JF. DNA damage produced by ionizing radiation in mammalian cells: Identities, mechanisms of formation, and reparability. *Prog Nucleic Acid Res Mol Biol*. 1988.
11. Sathishkumar S, Boyanovsky B, Karakashian AA, Rozenova K, Giltiay NV, Kudrimoti M, et al. Elevated sphingomyelinase activity and ceramide concentration in serum of patients undergoing high dose spatially fractionated radiation treatment. Implications for endothelial apoptosis. *Cancer Biol Ther*. 2005.
12. Dubois N, Rio E, Ripoche N, Ferchaud-Roucher V, Gaugler MH, Campion L, et al. Plasma ceramide, a real-time predictive marker of pulmonary and hepatic metastases response to stereotactic body radiation therapy combined with irinotecan. *Radiother Oncol*. 2016.
13. Paris F, Fuks Z, Kang A, Capodieci P, Juan G, Ehleiter D, et al. Endothelial apoptosis as the primary lesion initiating intestinal radiation damage in mice. *Science*. 2001;80.
14. Garnett CT, Palena C, Chakarborty M, Tsang KY, Schlom J, Hodge JW. Sublethal irradiation of human tumor cells modulates phenotype resulting in enhanced killing by cytotoxic T lymphocytes. *Cancer Res*. 2004;64.
15. Reits EA, Hodge JW, Herberts CA, Groothuis TA, Chakraborty M, Wansley EK, et al. Radiation modulates the peptide repertoire, enhances MHC class I expression, and induces successful antitumor immunotherapy. *J Exp Med*. 2006;203.
16. Verbrugge I, Gasparini A, Haynes NM, Hagekyriakou J, Galli M, Stewart TJ, et al. The curative outcome of radioimmunotherapy in a mouse breast cancer model relies on mTOR signaling. *Radiat Res*. 2014;182.
17. Sharabi AB, Nirschl CJ, Kochel CM, Nirschl TR, Francica BJ, Velarde E, et al. Stereotactic radiation therapy augments antigen-specific PD-1-mediated antitumor immune responses via cross-presentation of tumor antigen. *Cancer Immunol Res*. 2015;3.
18. Withers HR. The four R's of radiotherapy. 1975.
19. Dikomey E. The influence of the size of dose on the repair kinetics of X-ray-induced DNA strand breaks studied in CHO cells. 1993.
20. Moding EJ, Mowery YM, Kirsch DG. Opportunities for radiosensitization in the SBRT era. *Cancer J*. 2016;22.
21. Syljuåsen RG, McBride WH, Syljuasen RG. Radiation-induced apoptosis and cell cycle progression in jurkat T cells. *Radiat Res*. 1999;152.
22. Song CW, Lee YJ, Griffin RJ, Park I, Koonce NA, Hui S, et al. Indirect tumor cell death after high-dose hypofractionated irradiation: Implications for stereotactic body radiation therapy and stereotactic radiation surgery. *Int J Radiat Oncol Biol Phys*. 2015.
23. Fowler JF. The linear-quadratic formula and progress in fractionated radiotherapy. *Br. J. Radiol*. 1989.
24. McMahon SJ. The linear quadratic model: Usage, interpretation and challenges. *Phys Med Biol*. 2019;64.
25. Kirkpatrick JP, Meyer JJ, Marks LB. The linear-quadratic model is inappropriate to model high dose per fraction effects in radiosurgery. *Semin Radiat Oncol*. 2008;18.
26. Balkwill FR, Capasso M, Hagemann T. The tumor microenvironment at a glance. *J Cell Sci*. 2012;125.
27. Whiteside TL. The tumor microenvironment and its role in promoting tumor growth. *Oncogene*. 2008.
28. Sherwood LM, Parris EE, Folkman J. Tumor angiogenesis: Therapeutic implications. *N. Engl. J. Med*. 1971. pp. 1182–1186.
29. Folkman J. Tumor angiogenesis factor. *Cancer Res*. 1974.

30. Lamalice L, Le Boeuf F, Huot J. Endothelial cell migration during angiogenesis. *Circ. Res*. 2007.
31. Feng T, Yu H, Xia Q, Ma Y, Yin H, Shen Y, et al. Cross-talk mechanism between endothelial cells and hepatocellular carcinoma cells via growth factors and integrin pathway promotes tumor angiogenesis and cell migration. *Oncotarget*. 2017;8.
32. Tabas I. Secretory sphingomyelinase. *Chem Phys Lipids*. 1999.
33. Haimovitz-Friedman A, Kan CC, Ehleiter D, Persaud RS, McLoughlin M, Fuks Z, et al. Ionizing radiation acts on cellular membranes to generate ceramide and initiate apoptosis. *J Exp Med*. 1994.
34. Santana P, Peña LA, Haimovitz-Friedman A, Martin S, Green D, McLoughlin M, et al. Acid sphingomyelinase-deficient human lymphoblasts and mice are defective in radiation-induced apoptosis. *Cell*. 1996.
35. Peña LA, Fuks Z, Kolesnick RN. Radiation-induced apoptosis of endothelial cells in the murine central nervous system: Protection by fibroblast growth factor and sphingomyelinase deficiency. *Cancer Res*. 2000.
36. Gerweck LE, Vijayappa S, Kurimasa A, Ogawa K, Chen DJ. Tumor cell radiosensitivity is a major determinant of tumor response to radiation. *Cancer Res*. 2006.
37. Moding EJ, Castle KD, Perez BA, Oh P, Min HD, Norris H, et al. Tumor cells, but not endothelial cells, mediate eradication of primary sarcomas by stereotactic body radiation therapy. *Sci Transl Med*. 2015.
38. Ogawa K, Boucher Y, Kashiwagi S, Fukumura D, Chen D, Gerweck LE. Influence of tumor cell and stroma sensitivity on tumor response to radiation. *Cancer Res*. 2007.
39. Fulop GM, Phillips RA. The SCID mutation in mice causes a general defect in DNA repair. *Nature*. 1990.
40. Biedermann KA, Sun J, Giaccia AJ, Tosto LM, Brown JM. SCID mutation in mice confers hypersensitivity to ionizing radiation and a deficiency in DNA double-strand break repair. *Proc Natl Acad Sci U S A*. 1991.
41. Budach W, Hartford A, Gioioso D, Freeman J, Taghian A, Suit HD, et al. Tumors arising in SCID mice share enhanced radiation sensitivity of SCID normal tissues. *Cancer Res*. 1992.
42. Chang C, Biedermann KA, Mezzina M, Brown JM. Characterization of the DNA double strand break repair defect in SCID mice. *Cancer Res*. 1993.
43. Peña LA, Fuks Z, Kolesnick R. Stress-induced apoptosis and the sphingomyelin pathway. *Biochem. Pharmacol*. 1997.
44. Fuks Z, Haimovitz-Friedman A, Kolesnick RN. The role of the sphingomyelin pathway and protein kinase C in radiation-induced cell kill. *Important Adv. Oncol*. 1995.
45. Lomax ME, Folkes LK, O'Neill P. Biological consequences of radiation-induced DNA damage: Relevance to radiotherapy. *Clin Oncol*. 2013;25.
46. Mladenov E, Magin S, Soni A, Iliakis G. DNA double-strand break repair as determinant of cellular radiosensitivity to killing and target in radiation therapy. *Front. Oncol*. 2013.
47. Cannan WJ, Pederson DS. Mechanisms and consequences of double-strand DNA break formation in chromatin. *J. Cell Physiol*. 2016.
48. Zhao H, Zhuang Y, Li R, Liu Y, Mei Z, He Z, et al. Effects of different doses of X-ray irradiation on cell apoptosis, cell cycle, DNA damage repair and glycolysis in HeLa cells. *Oncol Lett*. 2019;17.
49. Lowe SW, Schmitt EM, Smith SW, Osborne BA, Jacks T. P53 is required for radiation-induced apoptosis in mouse thymocytes. *Nature*. 1993.
50. Czarnota GJ, Karshafian R, Burns PN, Wong S, Al Mahrouki A, Lee JW, et al. Tumor radiation response enhancement by acoustical stimulation of the vasculature. *Proc Natl Acad Sci U S A*. 2012.
51. El Kaffas A, Al-Mahrouki A, Hashim A, Law N, Giles A, Czarnota GJ. Role of acid sphingomyelinase and ceramide in mechano-acoustic enhancement of tumor radiation responses. *J Natl Cancer Inst*. 2018.
52. Jani A, Shaikh F, Barton S, Willis C, Banerjee D, Mitchell J, et al. High-dose, single-fraction irradiation rapidly reduces tumor vasculature and perfusion in a xenograft model of neuroblastoma. *Int J Radiat Oncol*. 2016.
53. Brown SL, Nagaraja TN, Aryal MP, Panda S, Cabral G, Keenan KA, et al. MRI-tracked tumor vascular changes in the hours after single-fraction irradiation. *Radiat Res*. 2015.
54. Song CW, Lee YJ, Griffin RJ, Park I, Koonce NA, Hui S, et al. Indirect tumor cell death after high-dose hypofractionated irradiation: Implications for stereotactic body radiation therapy and stereotactic radiation surgery. *Int J Radiat Oncol Biol Phys*. 2015.
55. Clement JJ, Tanaka N, Song CW. Tumor reoxygenation and postirradiation vascular changes. *Radiology*. 1978;127.
56. Kim MS, Kim W, Park IH, Kim HJ, Lee E, Jung JH, et al. Radiobiological mechanisms of stereotactic body radiation therapy and stereotactic radiation surgery. *Radiat Oncol J*. 2015;33.
57. Hill RP. Radiation-induced changes in the in vivo growth rate of KHT sarcoma cells: Implications for the comparison of growth delay and cell survival. *Radiat Res*. 1980.
58. Golden EB, Apetoh L. Radiotherapy and immunogenic cell death. *Semin. Radiat. Oncol*. 2015.
59. Apetoh L, Ghiringhelli F, Tesniere A, Criollo A, Ortiz C, Lidereau R, et al. The interaction between HMGB1 and TLR4 dictates the outcome of anticancer chemotherapy and radiotherapy. *Immunol. Rev*. 2007.
60. Poleszczuk J, Enderling H. The optimal radiation dose to induce robust systemic anti-tumor immunity. *Int J Mol Sci*. 2018.

61. Siemann DW. The unique characteristics of tumor vasculature and preclinical evidence for its selective disruption by tumor-vascular disrupting agents. *Cancer Treat. Rev*. 2011.
62. Bergers G, Song S. The role of pericytes in blood-vessel formation and maintenance. *Neuro Oncol*. 2005;7.
63. Park HJ, Griffin RJ, Hui S, Levitt SH, Song CW. Radiation-induced vascular damage in tumors: Implications of vascular damage in ablative hypofractionated radiotherapy (SBRT and SRS). *Radiat Res*. 2012;177.
64. Song CW, Levitt SH. Vascular changes in Walker 256 carcinoma of rats following X irradiation. *Radiology*. 1971;100.
65. Wong HH, Song CW, Levitt SH. Early changes in the functional vasculature of Walker carcinoma 256 following irradiation. *Radiology*. 1973;108.
66. Song CW, Payne JT, Levitt SH. Vascularity and blood flow in x-irradiated Walker carcinoma 256 of rats. *Radiology*. 1972.
67. Clement JJ, Tanaka N, Song CW. Tumor reoxygenation and postirradiation vascular changes. *Radiology*. 1978.
68. Zywietz F, Hahn LS, Lierse W. Ultrastructural studies on tumor capillaries of a rat rhabdomyosarcoma during fractionated radiotherapy. *Acta Anat (Basel)*. 1994;150.
69. Zywietz F, Reeker W, Kochs E. Tumor oxygenation in a transplanted rat rhabdomyosarcoma during fractionated irradiation. *Int J Radiat Oncol Biol Phys*. 1995.
70. Brurberg KG, Thuen M, Ruud E-BM, Rofstad EK. Fluctuations in pO_2 in irradiated human melanoma xenografts. *Radiat Res*. 2006.
71. Forster J, Harriss-Phillips W, Douglass M, Bezak E. A review of the development of tumor vasculature and its effects on the tumor microenvironment. *Hypoxia*. 2017;5.
72. Ng QS, Goh V, Milner J, Padhani AR, Saunders MI, Hoskin PJ. Acute tumor vascular effects following fractionated radiotherapy in human lung cancer: In vivo whole tumor assessment using volumetric perfusion computed tomography. *Int J Radiat Oncol Biol Phys*. 2007.
73. Mottram JC. A factor of importance in the radio sensitivity of tumours. *Br J Radiol*. 1936.
74. Gray LH, Conger AD, Ebert M, Hornsey S, Scott OC. The concentration of oxygen dissolved in tissues at the time of irradiation as a factor in radiotherapy. *Br J Radiol*. 1953;26.
75. Thomlinson RH, Gray LH. The histological structure of some human lung cancers and the possible implications for radiotherapy. *Br J Cancer*. 1955.
76. Nishida N, Yano H, Nishida T, Kamura T, Kojiro M. Angiogenesis in cancer. *Vasc. Health Risk Manag*. 2006.
77. Hinnen P, Eskens FALM. Vascular disrupting agents in clinical development. *Br. J. Cancer*. 2007.
78. Rajabi M, Mousa SA. The role of angiogenesis in cancer treatment. *Biomedicines*. 2017.
79. Wu XY, Ma W, Gurung K, Guo CH. Mechanisms of tumor resistance to small-molecule vascular disrupting agents: Treatment and rationale of combination therapy. *J. Formos. Med. Assoc*. 2013.
80. Mason RP, Zhao D, Liu L, Trawick ML, Pinney KG. A perspective on vascular disrupting agents that interact with tubulin: Preclinical tumor imaging and biological assessment. *Integr. Biol*. 2011.
81. Hofer E, Schweighofer B. Signal transduction induced in endothelial cells by growth factor receptors involved in angiogenesis. *Thromb Haemost*. 2007;97.
82. Fallah A, Sadeghinia A, Kahroba H, Samadi A, Heidari HR, Bradaran B, et al. Therapeutic targeting of angiogenesis molecular pathways in angiogenesis-dependent diseases. *Biomed. Pharmacother*. 2019.
83. Geel RMJM, Beijnen JH, Schellens JHM. Concise drug review: Pazopanib and axitinib. *Oncologist*. 2012;17.
84. Truman JP, García-Barros M, Kaag M, Hambardzumyan D, Stancevic B, Chan M, et al. Endothelial membrane remodeling is obligate for anti-angiogenic radiosensitization during tumor radiosurgery. *PLoS One*. 2010.
85. Rao SS, Thompson C, Cheng J, Haimovitz-Friedman A, Powell SN, Fuks Z, et al. Axitinib sensitization of high single dose radiotherapy. *Radiother Oncol*. 2014.
86. Teicher BA, Dupuis N, Kusomoto T, Robinson MF, Liu F, Menon K, et al. Antiangiogenic agents can increase tumor oxygenation and response to radiation therapy. *Radiat Oncol Investig*. 1994;2.
87. Teicher BA, Holden SA, Ara G, Dupuis NP, Liu F, Yuan J, et al. Influence of an anti-angiogenic treatment on 9L gliosarcoma: Oxygenation and response to cytotoxic therapy. *Int J Cancer*. 1995;61.
88. Griffin RJ, Williams BW, Wild R, Cherrington JM, Park H, Song CW. Simultaneous inhibition of the receptor kinase activity of vascular endothelial, fibroblast, and platelet-derived growth factors suppresses tumor growth and enhances tumor radiation response. *Cancer Res*. 2000;62.
89. El Kaffas A, Giles A, Czarnota GJ. Dose-dependent response of tumor vasculature to radiation therapy in combination with Sunitinib depicted by three-dimensional high-frequency power Doppler ultrasound. *Angiogenesis*. 2013.
90. Kaneko OF, Willmann JK. Ultrasound for molecular imaging and therapy in cancer. *Quant Imaging Med Surg*. 2012.
91. Liu Z, Gao S, Zhao Y, Li P, Liu J, Li P, et al. Disruption of tumor neovasculature by microbubble enhanced ultrasound: A potential new physical therapy of anti-angiogenesis. *Ultrasound Med Biol*. 2012;38.
92. Tran WT, Iradji S, Sofroni E, Giles A, Eddy D, Czarnota GJ. Microbubble and ultrasound radioenhancement of bladder cancer. *Br J Cancer*. 2012.

93. Al-Mahrouki AA, Iradji S, Tran WT, Czarnota GJ. Cellular characterization of ultrasound-stimulated microbubble radiation enhancement in a prostate cancer xenograft model. *DMM Dis Model Mech*. 2014.
94. Tarapacki C, Lai P, Tran WT, El Kaffas A, Lee J, Hupple C, et al. Breast tumor response to ultrasound mediated excitation of microbubbles and radiation therapy in vivo. *Oncoscience*. 2016.
95. Kim HC, Al-Mahrouki A, Gorjizadeh A, Karshafian R, Czarnota GJ. Effects of biophysical parameters in enhancing radiation responses of prostate tumors with ultrasound-stimulated microbubbles. *Ultrasound Med Biol*. 2013.
96. Al-Mahrouki A, Giles A, Hashim A, Kim HC, El-Falou A, Rowe-Magnus D, et al. Microbubble-based enhancement of radiation effect: Role of cell membrane ceramide metabolism. *PLoS One*. 2017.

2 Gamma Knife: From Single-Fraction SRS to IG-HSRT

Daniel M. Trifiletti, Jason Sheehan, and David Schlesinger

Contents

2.1 INTRODUCTION

Radiosurgery has traditionally been a high-dose, single-fraction treatment technique that has been found to be extremely effective for a large spectrum of malignant and benign neurosurgical conditions (Leksell, 1951). Delivery of high-dose radiotherapy in a single session leaves very little room for error, and as a result radiosurgery maintains a requirement for rigorous accuracy and precision management in treatment delivery. Gamma Knife (GK) radiosurgery (Elekta Instrument AB, Stockholm, Sweden) traditionally achieves this through the use of isocentric convergence of many small beamlets (201 or 192, depending on the model of the device) to create large-dose gradients and a rigid headframe that immobilizes the patient's head and defines a stereotactic coordinate system with a direct mechanical linkage between the patient's head and the isocenter of the Gamma Knife suitable for localization and targeting (Lunsford et al., 1988; Lindquist and Paddick, 2007). Image guidance has been based on up-front imaging of the patient using fiducial systems mounted to the patient's headframe to localize anatomy relative to the stereotactic frame of reference.

The development of radiosurgery did not end with the invention of the Gamma Knife, however. As experience accrued using linear accelerators as an alternative to the Gamma Knife for radiosurgery, it has become apparent that for certain clinical situations (for instance, tumors larger than what is typically indicated for radiosurgery or tumors directly adjacent to sensitive organs at risk [OARs]), delivery of the total dose over several fractions (hypofractionated stereotactic radiotherapy [HSRT]) creates some potential advantage, with similar tumoricidal effectiveness paired with further reduced normal tissue toxicity. The experience with linear accelerators also demonstrated the potential advantages to be gained by the use of in-room imaging techniques, making accurate and precise patient localization possible without the use of a rigid headframe and thereby making practical hypofractionated regimes.

Several techniques for both patient immobilization and image guidance have been developed that make hypofractionation on the Gamma Knife possible without compromising the historic precision characteristic

of GKRS. This chapter explores the technology of frameless image-guided HSRT using the Gamma Knife Perfexion with the Extend™ system (Elekta Instrument AB, Stockholm, Sweden), as well as the Gamma Knife Icon, with a focus on the technology of each system, the benefits and limitations, and the flexibility in workflow that each system supports. Additional potential HSRT platforms are explored in subsequent chapters.

2.2 TRADITIONAL GAMMA KNIFE RADIOSURGERY—SINGLE-FRACTION A PRIORI IMAGE-GUIDED RADIOSURGERY

2.2.1 IMMOBILIZATION

Traditional Gamma Knife radiosurgery is performed using a rigid stereotactic frame which is placed around the patient's head and fixed using four pins which are inserted to the outer table of the patient's skull. Frame placement is often performed in a small procedure room nearby the radiosurgery center, using local anesthetic to numb the pinsites as needed. Other centers prefer to administer light sedation in addition to the local anesthesia.

By design and definition, the stereotactic frame defines a coordinate system called the Leksell Coordinate System which has an origin superior, posterior, and right of the patient's head and increments towards the patient's left (+X), anterior (+Y), and inferior (+Z). The Leksell frame mounts mechanically to the treatment table on the Gamma Knife using an adapter in the case of the Perfexion (Figure 2.1), and therefore there is a mechanical correspondence between the stereotactic space defined by the frame and the coordinates of the Gamma Knife itself.

2.2.2 IMAGE GUIDANCE

Image guidance for traditional radiosurgery occurs a-priori of the procedure itself. Immediately following the frame placement, patients are generally sent for treatment planning imaging. The modalities involved may include MR, CT, and/or biplane angiography depending on the indication. Images are linked to the stereotactic coordinate system using modality-specific indicator boxes which are attached to the stereotactic frame during the imaging procedure. The indicator boxes result in fiducial markers in the resulting images, which, once they are registered with the treatment planning system, allow any point in the patient's brain anatomy to be referenced in stereotactic coordinate space (Figure 2.2 a, b). Non-stereotactic images (often

Figure 2.1 The Leksell stereotactic G-Frame attached to an anthropomorphic head phantom and docked to the Gamma Knife treatment bed. In addition to providing rigid immobilization, the stereotactic frame defines a coordinate system all over the patient's head that is mechanically linked to the machine coordinate system.

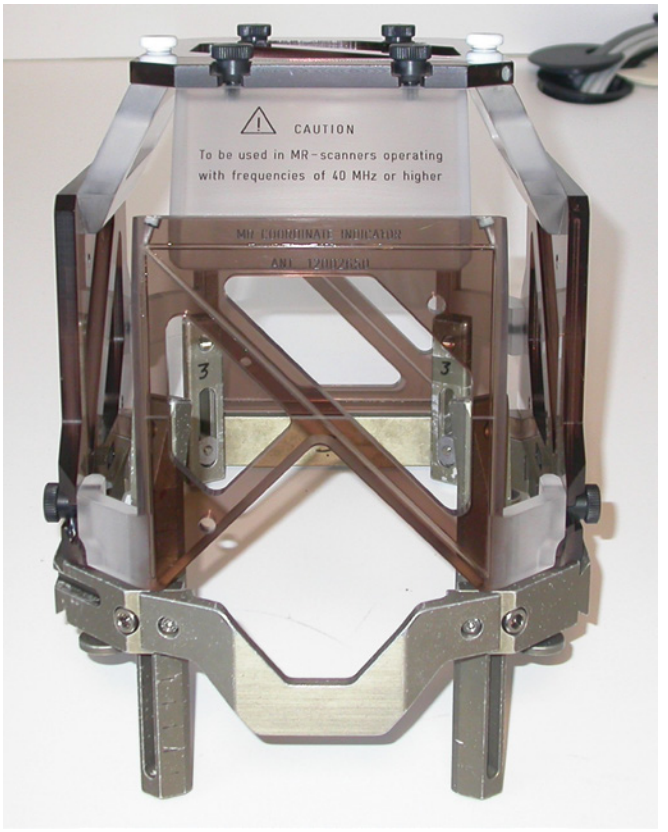

Figure 2.2a An MR indicator box mounted to a Leksell stereotactic frame. The indicator box channels are filled with copper sulfate solution that appears bright in MR images.

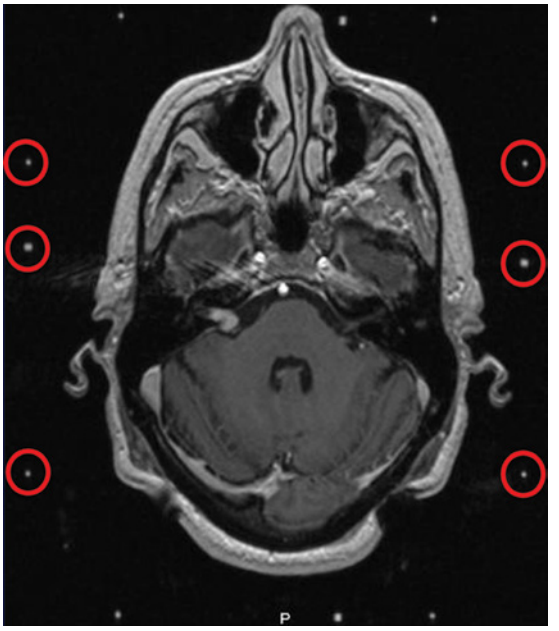

Figure 2.2b The fiducial marks (marked in red) on an MR image acquired with a stereotactic frame and MR indicator box.

including MR and/or PET) acquired prior to the frame placement are possible but must be co-registered to one of the stereotactic image studies to be useful.

2.3 LIMITATIONS OF TRADITIONAL GAMMA KNIFE SRS TECHNIQUES WHEN APPLIED TO IG-HSRT

There are several limitations to the traditional GK SRS frame, which limit its utility in HSRT. Most apparent is that the process of frame placement is invasive: pins are inserted into the outer table of the skull to create a rigid mechanical interface between the patient's head and the treatment machine. Moreover, this rigid association between the frame and the patient's skull is critical for the creation of the coordinate system used for localization and targeting, and any change in it invalidates the existing treatment plan.

A second limitation is that image guidance is a priori. This means that any change in the rigid association between frame and patient skull requires a new imaging study to re-establish the location of the patient anatomy relative to the coordinate system.

Beyond the inherent disadvantages of patient satisfaction, there are technical limitations to leaving a rigid head frame on for days as well. The presence alone of a rigid head frame does not ensure rigid fixation. Subtle shifts in the position of the head frame over the treatment course are possible, and daily measurements would be prudent to rule out these subtle systematic errors (either by digital probe or by imaging-based measurements).

2.4 REQUIREMENTS FOR GAMMA KNIFE IG-HSRT

2.4.1 ACCURACY AND PRECISION REQUIREMENTS

The most critical component of a hypofractionated immobilization system is that it can reliably and repeatedly localize the isocenter in three-dimensional space for each treatment fraction and that this localization must remain valid over the course of each treatment fraction. This tenant is the basis by which SRT is safe and feasible. A commonly acceptable tolerance for isocenter displacement is a non-systematic error of less than 1 mm. Although this tolerance is somewhat arbitrarily defined, there is evidence that adherence results in superior local control (Treuer et al., 2006). For the single-fraction case, the "gold standard" assumption has been that the rigid stereotactic frame provides superior immobilization performance over the relatively short time-frame required to deliver a radiosurgical treatment. Given the small geometric distances between tumor and sensitive OARs in the brain, any image-guided hypofractionated stereotactic radiation therapy (IG-HSRT) system cannot deviate far from the single-fraction standard.

2.4.2 REQUIREMENT FOR PATIENT ACCEPTANCE

A possibly overlooked component of rigid immobilization is that it is must be reasonably well tolerated by patients. Patient satisfaction has become a critical component of medical care, and other fractionated radiotherapy approaches (i.e., gynecologic brachytherapy) have led to psychosocial disorders in some patients, thought to be related to the discomfort of the applicator left in place between fractions (Kirchheiner et al., 2014). Any IG-HSRT system that limits patient discomfort would also lead to less inter- and intrafraction motion, require less intrafraction treatment breaks, and have faster daily patient set up.

2.4.3 REQUIREMENT FOR SOME POTENTIAL TO EXPAND INDICATIONS

Traditional single-fraction Gamma Knife radiosurgery has been a remarkably successful technique, with over 1.3 million patients treated worldwide between 1968 and 2019, with 95,000 treated in 2019 alone (Leksell Gamma Knife Society, 2019). A successful system for hypofractionated Gamma Knife treatments requires a rationale that creates an expansion of indications beyond those already effectively managed with the current system.

There is a great potential in a method of reliable GK immobilization and hypofractionation. As described in other chapters, HSRT would increase the scope of SRT by permitting radiosurgery in anatomic locations that have previously been treated with conventionally fractionated radiotherapy because of concern of adjacent normal tissue tolerance. Additionally, it is possible that some intracranial tumors have

a biology that would demonstrate improved local control with multi-fraction radiosurgery (Jee et al., 2014; Minniti et al., 2014; Toma-Dasu et al., 2014; Casentini et al., 2015).

2.5 HISTORICAL ATTEMPTS TO HYPOFRACTIONATE RADIOSURGERY TREATMENTS

There have been a variety of historical attempts both within and outside the Gamma Knife subspecialty to create methods that could allow for hypofractionation. This section summarizes some historical attempts which form the basis for modern GK-HSRT.

2.5.1 PROTRACTED FRAME APPLICATION

The feasibility of this method was first reported by Simonová in the early 1990s as a method to achieve hypofractionated stereotactic radiotherapy while only utilizing available devices (Simonova et al., 1995). They reported on 48 patients who underwent head frame placement and then returned for once daily treatments for 2 to 6 days. The method was considered feasible, well tolerated, and relatively safe. However, patients were admitted for the duration of therapy, making this an expensive treatment option. Additionally, patient-reported outcomes were not included in this report. A similar "split-dose" approach was reported where the total SRS dose was divided into two equal fractions. Patients underwent frame placement, imaging for treatment planning, and then first treatment fraction in the evening of the first day, followed by a second fraction delivered approximately 14–15 hours later. The authors of the study reported that the treatment was well tolerated and showed a small survival benefit for patients receiving two-fraction SRS as compared to an earlier cohort receiving single-fraction SRS. However, the authors cautioned against the possibility of a frame becoming dislodged over the total time of the procedure (Davey et al., 2007).

2.5.2 REMOVABLE FRAME SYSTEMS

The TALON cranial fixation system (Nomos Corp., Sewickley, PA) is a removable frame system that permits rigid fixation of the skull to a head frame through attachment to base screws inserted into the patient's skull. These screws are attached to the TALON system and permit minute adjustments of the cranium after fixation. The screws are left in place between fractions (usually 2 to 5 days). Salter et al. reported on the TALON system's positional accuracy and estimated that 95% of true isocenter position between fractions would fall within 1.55 mm of the planned isocenter position. The TALON system was well tolerated by patients; however, three of nine patients included developed infections at the screw sites, and two patients had loosening of the screws between fractions requiring re-tightening (Salter et al., 2001). The TALON system was not attempted in a Gamma Knife SRT context.

2.5.3 RELOCATABLE FRAME SYSTEMS

Multiple relocatable head frame systems have been developed over the past 15 years. This includes rigid frames used for radiosurgery registration, which are not invasively attached to the patient (Reisberg et al., 1998; Alheit et al., 1999; Ryken et al., 2001; Baumert et al., 2005; Minniti et al., 2010; Ruschin et al., 2010). Examples include systems that have utilized bite blocks, head straps, thermoplastic masks, optical tracking, or some combination. In all cases, the important characteristics include relatively simple, noninvasive methods for placing the patient in a repeatable treatment position corresponding to the position at the time of treatment planning.

2.6 HISTORICAL DEVELOPMENT OF ONBOARD IMAGE GUIDANCE FOR RADIOSURGERY

The development of in-room image-guidance systems for radiotherapy was a significant development that enhanced the accuracy and precision by which a patient could be set in the correct treatment position. These systems, designed primarily for linear accelerator-based radiotherapy, were quickly adapted for use in radiosurgery contexts. Systems evolved from simple 2D MV portal imaging systems that used film (and later flat-panel detectors) that were exposed by the treatment beam to allow clinicians to verify whether the

target was within the collimated field (Dong et al., 1997). The invention of amorphous-silicon flat-panel detectors motivated attempts to use the treatment machine itself as an megavoltage cone beam CT system (Pouliot et al., 2005). kV-CBCT systems were developed using x-ray tubes and detectors mounted orthogonally from the LINAC treatment beam (Jaffray, 2007). Dual ceiling/floor-mounted stereoscopic kV x-ray systems were developed specifically for radiosurgery applications.

The aforementioned developments for linear accelerators were motivated as much for extracranial stereotactic and non-stereotactic indications as they were for intracranial indications, as the stereotactic frame was a well-established and well-validated technique for intracranial radiosurgery. However, as noted earlier, an enhanced ability to hypofractionate is considered advantageous in certain clinical situations. To that end, David Jaffray's group at Princess Margaret Hospital developed a kV-CBCT system that they successfully integrated with a Gamma Knife Perfexion. The system uses a conventional 90 kVp rotating anode x-ray tube and an opposing detector. The system is supported by a set of vertical supports, which allows the system to translate from a parked position above the shield-doors of the Perfexion to an imaging position between the patient and the shield-doors. A rotational axis allows the system to rotate by 210° for imaging. Isotropic voxel resolutions (1mm or 0.5 mm) are achievable with a reconstruction field of view of 25.6 × 25.6 × 19.3 cm (Ruschin et al., 2013).

2.7 EXTEND SYSTEM FOR THE GAMMA KNIFE PERFEXION

While the previous section summarizes work that has been performed to explore options for GK IG-HSRT, the first clinically available commercial solution in practice to allow for hypofractionated Gamma Knife radiosurgery treatments was the Extend system (which at the time of publication of this edition is not actively marketed but is supported and clinically deployed). The Gamma Knife Extend System made reproducible, frameless stereotactic fixation of the head possible through a suctioned dental mold of the hard palate and maxillary teeth. The system removed the requirement for surgical intervention needed for frame placement, and no devices were left *in situ* between fractions, which could cause pain or serve as a nidus for infection (Ruschin et al., 2010).

2.7.1 MAIN COMPONENTS

The Extend frame system consists of a carbon-fiber front plate to which a dental impression/mouthpiece can be attached, a base plate to which the front-piece can be attached, and a vacuum cushion on which the patient's head sits. The Extend frame rigidly docks with the GK patient positioning system (PPS).

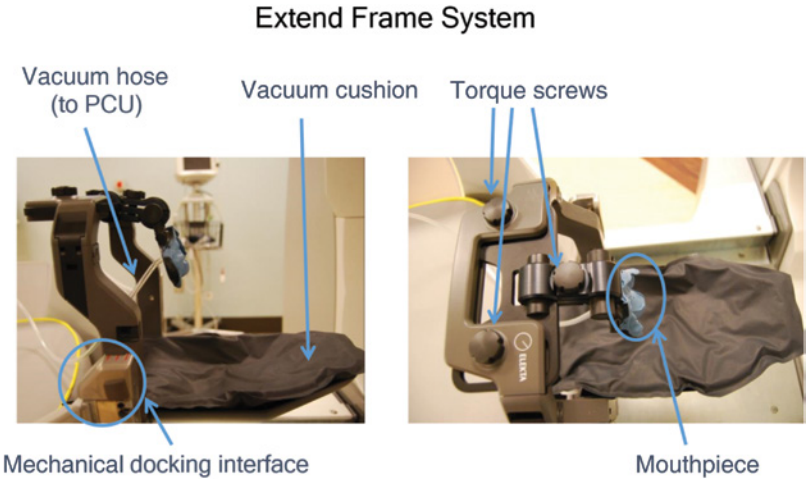

Figure 2.3 The Extend Frame system and its components.

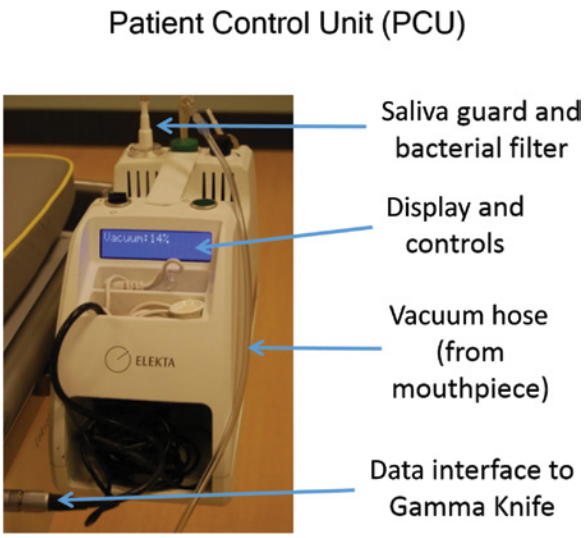

Figure 2.4 The Patient Control Unit (PCU) for the Gamma Knife Extend system. The PCU creates a vacuum that is used to monitor patient movement and sends data during treatment to the Gamma Knife control system to interrupt treatment if the vacuum level falls below a set threshold.

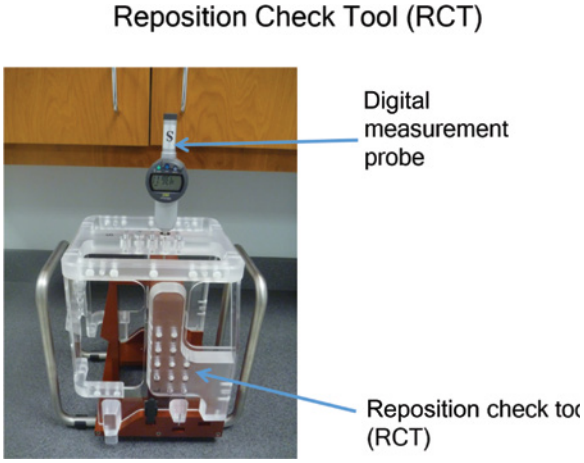

Figure 2.5 The reposition check tool (RCT) template and associated digital measurement probe. The red carrier doubles as a QA tool for the RCT.

The mouthpiece of the frame is attached via plastic tubing to the Patient Control Unit (PCU). The PCU consists of a vacuum pump and tubing that connects to the mouthpiece and interfaces with the patient and the treatment unit. The reposition check tool (RCT) consists of an acrylic measurement template and an associated set of digital measurements probes. The RCT fits into slots on the Extend frame. Measurement holes in the RCT template are used for the measurement of head position to confirm three-dimensional positioning between fractions.

2.7.2 DENTAL MOLD CREATION

The first step in the use of the Extend system is the selection of the mouthpiece and the creation of the dental mold. A dental impression is created using standard impression material (vinyl polysiloxane) using a mixing gun. A plastic spacer is placed between the mold and the hard palate before inserting the

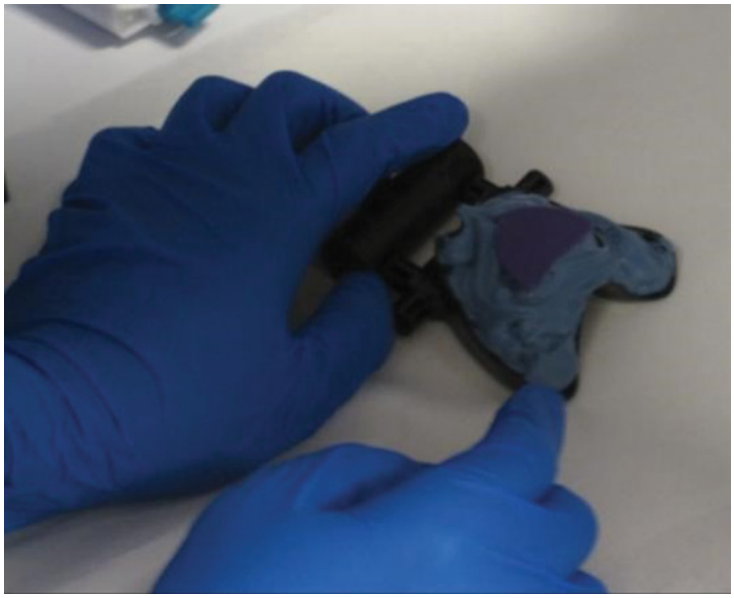

Figure 2.6 Creation of an Extend system dental impression. The impression material fills a mouthpiece, and the plastic spacer (in purple) creates a vacuum space within the dental material.

Figure 2.7 Placement of an Extend system mouthpiece in a patient's mouth. Even pressure must be applied for several minutes while the impression material cures. (Patient's face blurred for confidentiality.)

mouthpiece into the patient's mouth to create the impression. The spacer allows for an air space in which the vacuum can suction the mold to the palate, aligned by dental anatomy (Figure 2.6). Once the mouthpiece is placed in the patient's mouth, even pressure must be maintained along the palate to allow the impression material to cure (Figure 2.7). If there is insufficient material between the teeth and the mouthpiece or between the hard and soft palate, then reliable suction may be difficult. In addition, edentulous patients or patients without adequate dentition are contraindicated for Extend immobilization.

2.7.3 SETUP AT GAMMA KNIFE

Creation of the dental impression is followed by setup at the Gamma Knife and the construction of the Extend frame system using the completed mouthpiece.

2.7.3.1 Dental Mold Insertion/Frame Creation

The patient is placed in a comfortable position on the Gamma Knife treatment bed. The dental mold connection with the spacer and vacuum tubing is confirmed and is guided into the patient's mouth and abutted to the hard palate and maxillary dentition. The PCU vacuum is then tested with the mouthpiece in place to a vacuum level of 30% to 40% (as a percentage of atmospheric pressure). The PCU has a safety alarm that can detect a loss of suction (defined as a 10% change in suction from the set point).

With the dental mold in place and the vacuum activated, the head frame can be secured. This is first done by attaching the front piece to the mold and then by locking the front piece to the docking area (which is locked to the GK couch). When patient comfort is again confirmed, the mouthpiece and head frame are hand tightened and then secured with a torque wrench (Figure 2.8).

2.7.3.2 Vacuum Cushion Creation

In the supine position with the head frame attached, the vacuum cushion is molded to the scalp, and the PCU is used to evacuate air from the cushion. As the vacuum level in the cushion increases, the cushion becomes increasingly rigid and molded to the shape of the patient's head. When complete, the result is a rigid cushion containing a firm impression of the dorsal aspect of the scalp that will be maintained for each fraction.

2.7.3.3 Test Measurements/RCT Measurement Hole Selection

The completed patient-specific dental impression, frame, and vacuum cushion define the stereotactic alignment of the patient's head with the couch.

To confirm proper alignment of the head within the frame, daily reference measurements are taken using the reposition check tool (RCT) and are compared to measurements taken at the time of

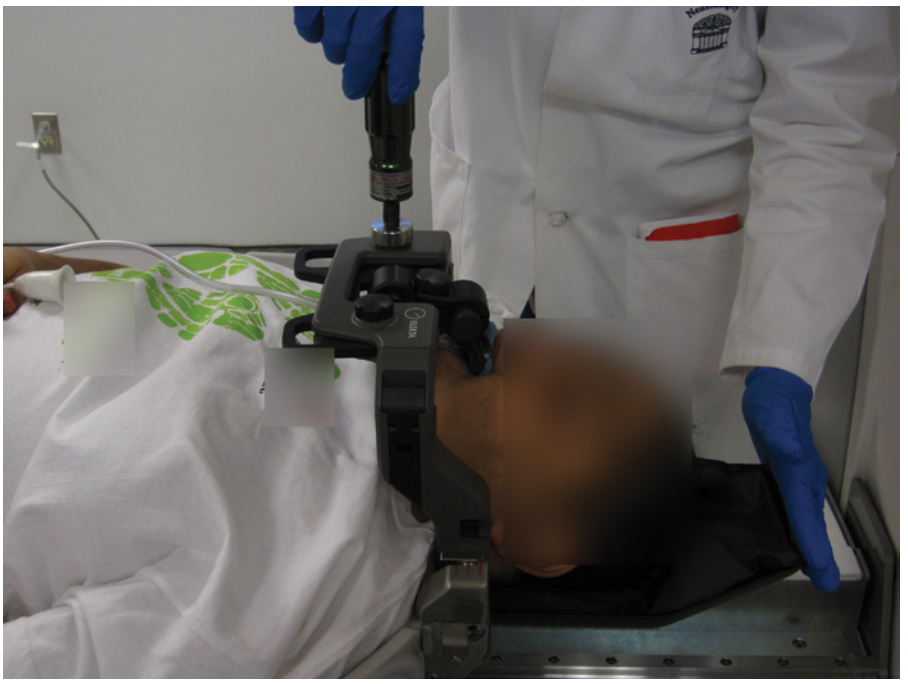

Figure 2.8 Creation of a patient-specific Extend frame by tightening the locking screws on the frame front plate with a torque wrench. (Patient's face blurred for confidentiality.)

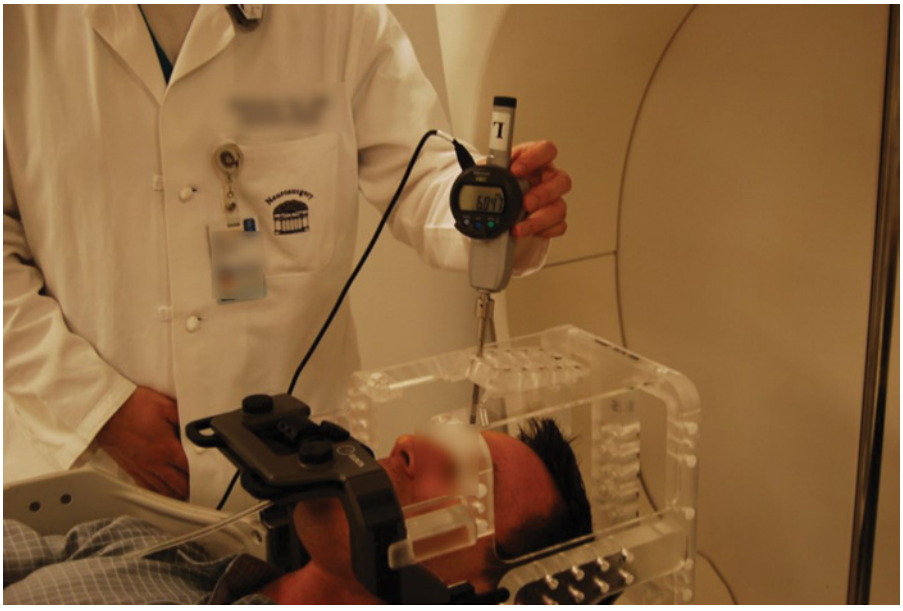

Figure 2.9 Physician acquiring reposition measurements using the RCT and the digital probe system.

image acquisition (computed tomography [CT] or magnetic resonance imaging [MRI]). During this initial setup step, RCT apertures are chosen for the measurements, and the distances to the head are recorded on a worksheet. The RCT consists of four plastic panels that surround the patient's head in the Extend frame (Figure 2.9). Measurements are taken with a pair of electronic linear measurement probes that are included in the Extend system (C150XB Digimatic Indicator, Mitutoyo Corp.). The probes measure the distance between preset holes in the RCT and the scalp. At least one aperture (and ideally more than one) must be chosen for each panel of the RCT. Apertures should be chosen to ideally allow normal incidence of the probe tips to the patient's head. Choosing apertures far apart from each other and avoiding areas of loose skin or fat can improve the precision and reproducibility of measurements.

It is important to note that any change in the vacuum pressure of the mouthpiece, of the vacuum cushion, or of the tension in the screws of the head frame can result in compromise of the rigidity and reproducibility of the Extend system. If these changes occur, the system should be reset from the beginning.

2.7.4 SIMULATION (CT) IMAGING

Following initial setup at the Gamma Knife, patients proceed to simulation imaging which will serve as the reference stereotactic images for treatment planning.

2.7.4.1 Simulation Imaging Setup and Reference RCT Measurements

The basic principle of the Extend system is that the patient position at the time of treatment must match (to within a small uncertainty threshold) the patient position at the time of simulation imaging. Therefore, at the time of stereotactic CT imaging, reference measurements are collected that will serve as the standard to compare future measurements to (prior to each treatment delivery). The process begins with the stereotactic immobilization of the patient as outlined earlier, but it is done on the CT couch as opposed to the GK couch. During any period that the head frame is assumed to be rigidly fixed, the PCU should be set to alarm for changes in vacuum, and the patient should be visually monitored to ensure comfort, as hand signals are preferred while the mouthpiece is in place. Measurements proceed as described earlier, using the measurement apertures chosen at the time of initial setup at the Gamma Knife. These measurements are read off of the display on the PCU and recorded on a worksheet for later use.

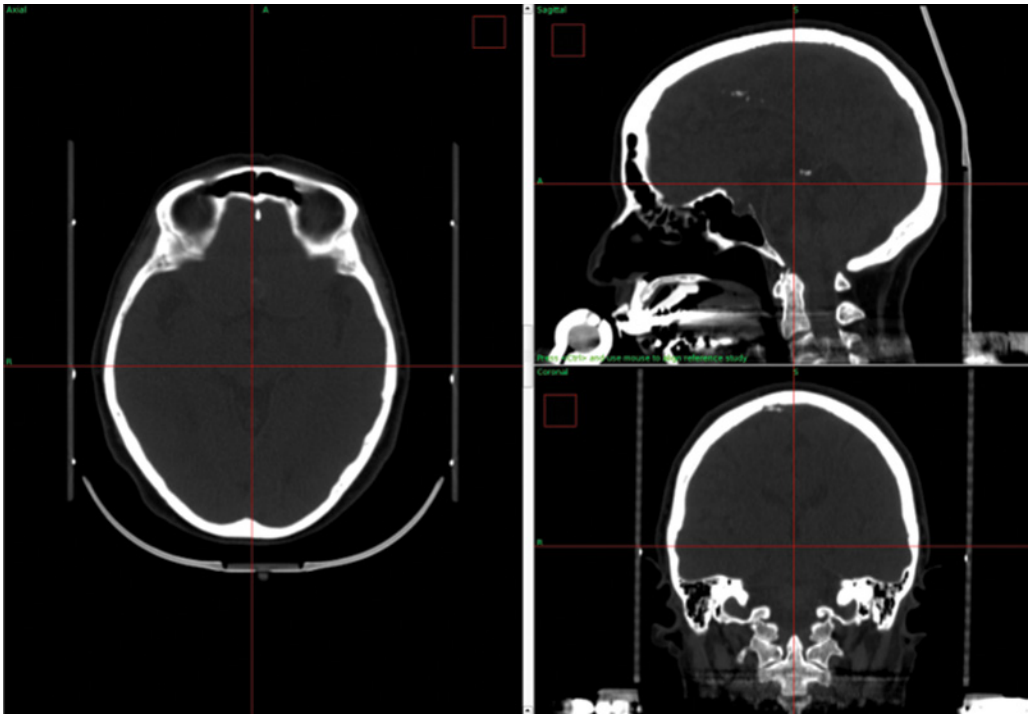

Figure 2.10 Stereotactic CT of an Extend patient. The CT field of view must cover the entire head and include the lateral fiducial markers.

2.7.4.2 Simulation Stereotactic CT Imaging

After proper immobilization is achieved and RCT measurements confirmed and recorded, the Extend CT indicator box is mounted to the frame. The CT indicator is a transparent box with implanted fiducial markers that can serve as rigid points in the GK treatment planning software (TPS, GammaPlan, Elekta AB, Stockholm, Sweden). CT images of the head are then obtained from vertex to mid-frame and with a field of view wide enough to include the entire CT indicator and corresponding fiducial markers (Figure 2.10). Intravenous contrast can be utilized as clinically indicated.

2.7.4.3 Post-CT Measurements

Immediately after the CT sequences are obtained and before releasing the vacuum suction, post-CT measurements with the RCT are important to verify that the patient did not shift during CT imaging. This is done by the same method as described earlier, through the same apertures as were used in the pre-CT measurements. Any difference of more than 0.5 mm from the pre-CT value should prompt the team to remove and reposition the Extend head frame, re-measure, re-obtain CT images, and then confirm measurements. After the repeat measurements are verified, the suction can be released and the head frame removed. Images are then transferred to the Gamma Knife treatment planning system.

2.7.5 INTEGRATION OF NON-STEREOTACTIC SCANS

The Extend system requires that a stereotactic CT be used as a stereotactic reference. CT images are less likely to suffer from localized geometric distortion, and the Extend frame does not fit within all MR head coils—two considerations which may be the source for this requirement. However, multimodality images (especially MR) are critical for the visualization of most intracranial indications, so non-stereotactic images may be incorporated into treatment planning via image registration. The Gamma Knife treatment planning system includes cross-modality rigid co-registration algorithms for this purpose (Viola and Wells III, 1997).

2.7.6 TREATMENT PLANNING

After all stereotactic and non-stereotactic imaging has been imported into the Gamma Knife treatment planning system, the stereotactic CT images are registered to stereotactic space using the fiducial markers visible in the CT images. MR and other modality images are then co-registered to the reference CT images as described earlier. The details of target visualization and delineation vary by institution; however, the planning includes functionality to delineate target volume(s) and adjacent organs at risk (OARs) similar to traditional SRT planning. Isocenter-based "shots" are placed and customized based on target size, shape, and adjacent OARs (Figure 2.11). Total dose and the number of fractions are entered, and the plan is reviewed by the neurosurgeon, medical physicist, and radiation oncologist.

2.7.7 TREATMENT PROCEDURE

2.7.7.1 Entering Reference Measurements (1st Fraction)

When a patient treatment is started at the Gamma Knife console prior to delivery of the first treatment fraction, the system requires that the reference position measurements acquired at the time of CT imaging be entered into the system. Accuracy at this step is critical because it will create a reference point to which each fraction will be directly compared. As such the reference measurements should be carefully double checked (preferably by a separate member of the team) prior to moving forward.

2.7.7.2 Repositioning Measurements

When the patient is prepared to proceed with therapy, they should enter the GK vault and have the Extend treatment head attached in a manner similar to when it was attached prior to CT-simulation (supine, vacuum cushion in place, mouthpiece, vacuum, front piece, secure to couch). Then new measurements should be collected using the electronic probe though the same apertures that were used for the reference measurements. This process is guided by the GK Extend console, which automatically captures each probe measurement and compares to the previously entered reference measurements. Once all selected RCT apertures have been measured, the console software will calculate a three-dimensional translational vector of the difference in patient position as compared to the reference measurement. The system will warn the operator if the radial positional difference is greater than 1.0 mm and suggest the clinician consider repositioning to

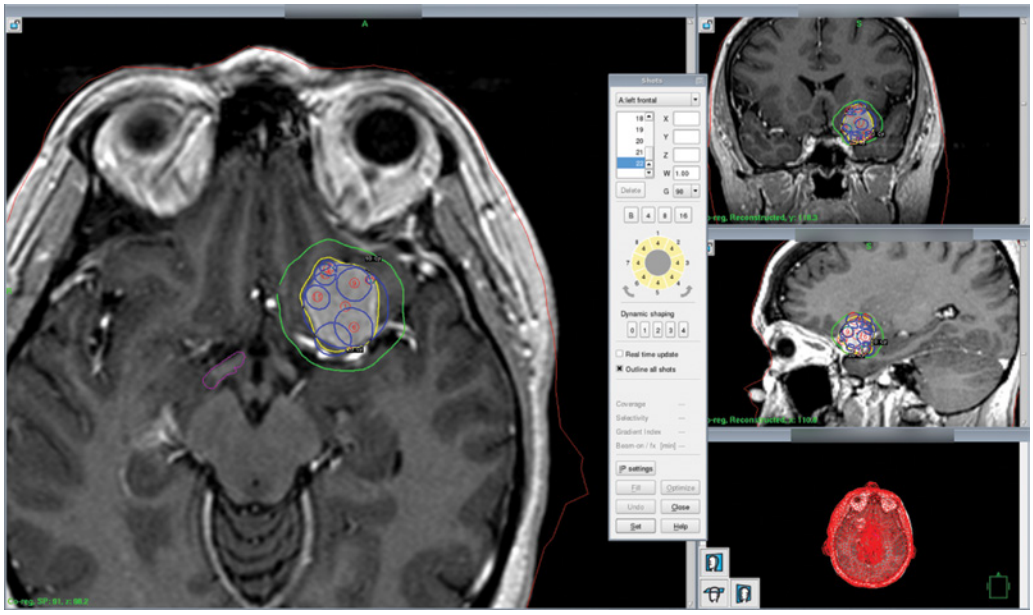

Figure 2.11 A treatment plan for a hypofractionated Gamma Knife radiosurgery case using the Extend system.

achieve a more favorable patient position. However, clinical judgment is ultimately involved in determining what level of positional uncertainty is acceptable.

2.7.7.3 Treatment

Following patient positioning, each individual SRT treatment is administered in the same way as a single-fraction Gamma Knife treatment. The Gamma Knife treatment couch translates the patient's head into the center of the radiation body of the unit, placing the patient's head at a location corresponding to the coordinates of each shot of the treatment plan in turn. Each position is maintained for a dwell duration as calculated by the treatment planning system in order to achieve the desired overall dose distribution. Treatments are monitored by the operator of the machine via video and audio surveillance. The patient is provided with a call button to alert the operator if they require assistance as the patient cannot speak with the Extend mouthpiece in place. It can be useful for the treatment team (usually a radiation therapist, medical physicist, neurosurgeon, and radiation oncologist) to develop a set of hand gestures that provide general communication.

2.7.7.4 Intrafraction Position Monitoring

Patient immobilization is monitored using the PCU vacuum surveillance system. Patient motion beyond a very small threshold will trigger a loss of suction in the Extend mouthpiece. Any loss of vacuum greater than 10% of vacuum level set at the time of patient positioning will trigger an interrupt which will shield the Gamma Knife 60Co sources and pause the treatment, automatically withdrawing the patient from the treatment position in the machine. This occurrence requires that the patient position be re-measured using the RCT and probe system and repositioned if required before the treatment can resume. If adequate repositioning is impossible, then a new stereotactic CT may be acquired and the treatment plan shifted to accommodate the new patient position.

2.7.8 ACCURACY COMPARED TO SIMILAR SYSTEMS

The mean setup uncertainty of the Gamma Knife Extend system has been shown to be reproducibility on the order of 0.4 to 1.3 mm (Ruschin et al., 2010; Sayer et al., 2011; Schlesinger et al., 2012; Ma et al., 2014). Table 2.1 reports the mean displacement of the patient after setup by a representative variety of proposed immobilization systems applicable to fractionated radiosurgery. As demonstrated, the setup uncertainty of the Extend system is comparable to other available relocatable frame systems.

Table 2.1 Reports of the residual setup uncertainty of a variety of relocatable immobilization systems for fractionated radiation treatments

AUTHOR	DEVICE	SETUP DISPLACEMENT, MM (SD)
(Sweeney et al., 1998)	Bite block + vacuum assist	<1.02*
(Rosenberg et al., 1999)	GTC frame	1.1 (0.6)#
(Ryken et al., 2001)	Mask + optically tracked bite block	0.16 (0.04)†
(Baumert et al., 2005)	Mask + bite block	2.2 (1.1)‡
(Kunieda et al., 2009)	Bite block + vacuum assist	0.93–1.09 (0.52–0.88)‡
(Minniti et al., 2010)	Relocatable frame + upper jaw support	0.5 (0.4)‡
(Ruschin et al., 2010)	Extend prototype	1.0^ / 1.3†
(Schlesinger et al., 2012)	Extend clinical system	0.64 (0.25)^

Note: Symbols indicate basis for setup displacement measurement (* fiducials versus surface landmarks; # orthogonal radiograph landmarks; † fiducials versus CBCT; ‡ simulation CT versus QA CT; ^ probe/depth measurements).

Source: Table adapted from Schlesinger et al., (2012).

2.7.9 LIMITATIONS OF EXTEND SYSTEM

The Extend system provides a reliable, noninvasive method for reproducible immobilization of patients for HSRT. However, as compared to HSRT systems for other treatment devices, the Extend system may have some potential limitations.

2.7.9.1 Complicated Workflow

One drawback to the Extend system is the complex logistic aspect of the mouthpiece creation, application, and RCT measurement system. The mouthpiece can be bulky and must fit snuggly and firmly for the frame to be reliably fixed. Generally, patients consider the first day of treatment arduous because dental mold creation, head frame fitting, CT, planning, first fraction, and numerous precise measurements can take hours to complete with the head frame in place. However, subsequent treatments are considered relatively convenient (Sayer et al., 2011).

2.7.9.2 Vacuum as a Proxy for Motion

The basis of the real-time monitoring of the Extend system is in the vacuum alert. The system relies on the assumption that any change in the vacuum pressure of greater than 10% equates to a displaced target. It does not detect possible patient motion in which the vacuum level changes by less than 10%. Conversely, the vacuum alert assumes that any change in vacuum of greater than 10% means that the patient moved systematically (as opposed to no movement or temporary movement). Additionally, after the alert is activated, it is impossible to tell if the change in pressure was indeed related to patient movement or potentially equipment failure in the vacuum or tubing, and the confirmation of functional equipment is warranted for unexpected vacuum alarm. In any case, the activation of the vacuum alarm results in a treatment pause, and the entire head frame should be removed, replaced, and re-measured to ensure proper placement and treatment accuracy.

2.7.9.3 Patient Contraindications (Dentition/Performance Status/Gag)

For a patient to be eligible for HST using the GK Extend system, they should be otherwise fit for radiosurgery (limited number of intracranial targets, adequate performance score, etc.). Although it should be noted that there are some aspects of the Extend system that may require additional patient cooperation compared to a standard head frame. Patients with a sensitive gag reflex may not be willing or able to tolerate a bulky mouthpiece for the duration of multiple treatments. Also as discussed previously, adequate dentition is critical to the reproducibility of the dental mold placement.

2.8 IG-HSRT WITH GAMMA KNIFE® ICON™

The Extend system proved to be a practical, if somewhat cumbersome, method for achieving a hypofractionated Gamma Knife technique. However, the system was limited in scope and functionality relative to comparable systems routinely used in Linac-based radiosurgery. Recognizing that the Extend system would not be an optimal solution on its own, Elekta Instrument, AB, the manufacturer of the Gamma Knife, began a development cycle intending to address some of the shortcomings of the Extend system for IG-HSRT. In particular, they redesigned and commercialized a prototype created at the University of Toronto (Ruschin et al., 2013) and created a new treatment solution with an integrated capability to verify and monitor patient position before and during treatment. This ultimately resulted in a new Gamma Knife platform, Gamma Knife Icon. Gamma Knife Icon replaces the older Extend system as a Gamma Knife IG-HSRT solution. The new system discards the cumbersome dental-impression-based frame in favor of thermoplastic mask immobilization; however, it also includes features that improve single-fraction G-frame treatments.

2.8.1 MAIN COMPONENTS

Gamma Knife Icon adds several new components to the Gamma Knife Perfexion platform. The most conspicuous addition is that of a CBCT mounted to the side of the unit. The system also includes a stereoscopic optical tracking system consisting of a folding infrared camera system mounted near the foot of the Gamma Knife PPS that is aimed toward the head of the unit. A new headrest is included that holds a

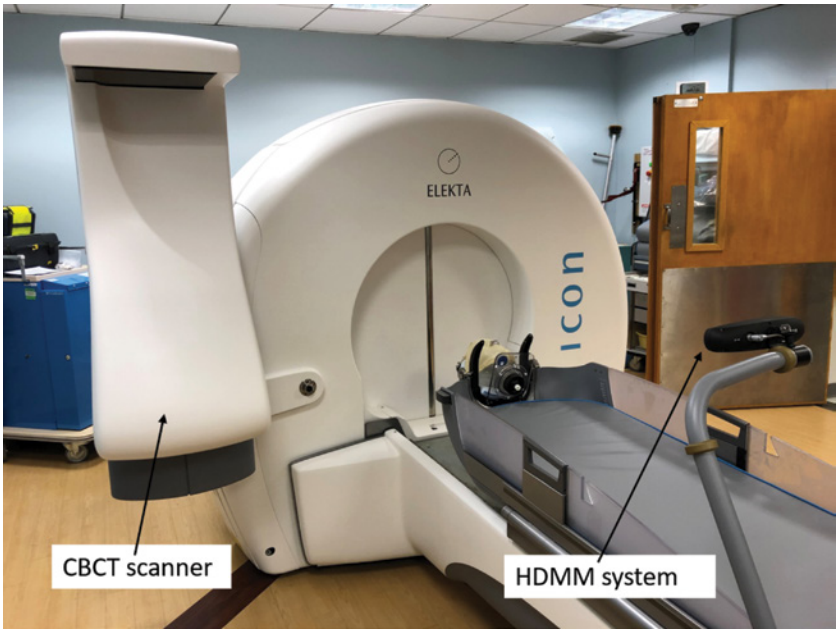

Figure 2.12 The Gamma Knife Icon system. Annotations show the onboard CBCT scanner and the High-Definition Motion Management (HDMM) infrared system.

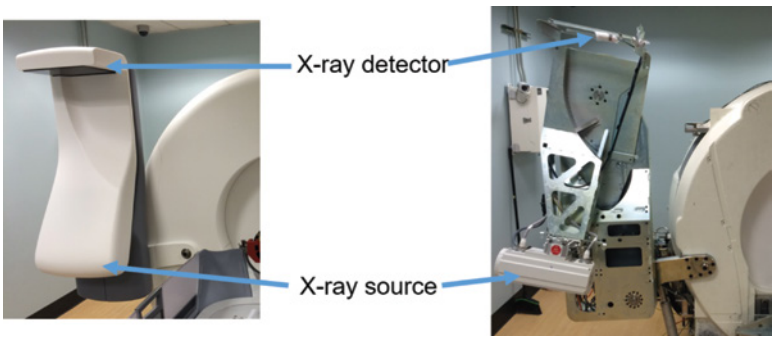

Figure 2.13 The Gamma Knife Icon CBCT system. Left: CBCT gantry with plastic covers intact. Right: CBCT gantry with plastic covers removed. Note: The flat-panel detector has been removed in the picture on the right.

patient-specific pillow, acts as a mount for a thermoplastic mask, and contains four infrared reflectors on rigid posts that act as reference markers for the patient position as described later (Figure 2.12).

The CBCT system is designed specifically for the task of determining the patient's stereotactic position both at time of initial setup and before each treatment session (Figure 2.13). The CBCT has 200 degree rotation, an imaging volume of 448 cm^3, 0.5 mm voxel size, and a resolution of more than 7 line pairs/cm, using 332 projections at 90 kVp. The system has two imaging modes distinguished by their nominal computed tomography dose index; high-dose mode has a CTDI of approximately 6.5 mGy and has a slightly higher signal-to-noise ratio as compared to the low-dose mode with a CTDI of 2.3 mGy. Most importantly, the CBCT isocenter has a known geometrical relationship with the radiation isocenter of the unit, determined through a calibration and quality assurance procedure (AlDahlawi et al., 2017). CBCT scans acquired with the system are therefore in stereotactic coordinate space. Preliminary tests on localization uncertainty using a phantom suggest a mean positional uncertainty of less than 0.2 mm (Eriksson and Nordström, 2014; Eriksson et al., 2014).

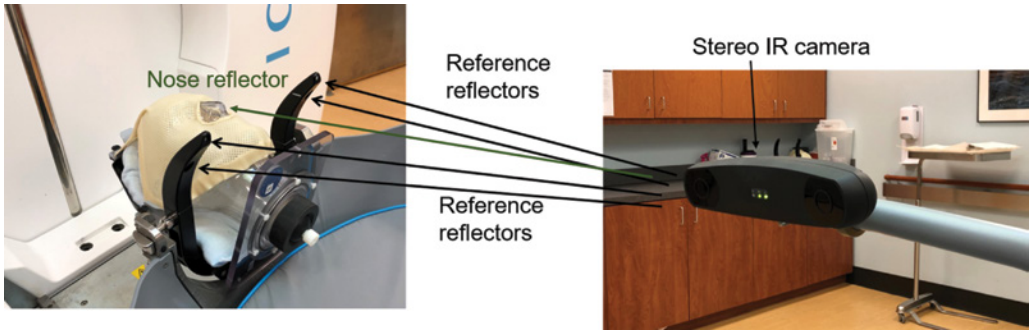

Figure 2.14 A close-up of the HDMM system. Right: A close-up view of the stereo infrared camera system. Left: A close-up view of the patient headrest/marker system with an anthropomorphic phantom setup. The system tracks the nose marker relative to the four reference markers found on the posts on each side of the headrest.

The optical imaging system, named the HDMM System, uses a stereoscopic infrared camera unit to track patient motion. The system is mounted near the foot of the PPS on a folding arm. When raised, the camera system has a view of a newly developed headrest that mounts to the head of the PPS in a manner similar to the stereotactic frame adapter for frame-based procedures. The headrest has lateral posts, each with two infrared-reflective markers that together serve as a static positional reference for the tracking system. During procedures, a fifth marker is placed on the patient's nose, and the system differentially tracks patient position relative to the four static markers (Figure 2.14). Phantom studies have reported a motion resolution of 0.06 mm (Wright et al., 2017).

Gamma Knife Icon is designed in a way that makes an in-field upgrade of the existing Gamma Knife Perfexion systems possible. The radiation body and collimator design of the two models are identical; the upgrade involves mounting the CBCT system to the radiation body, the HDMM system to the PPS bed, removal of the Extend system components (if applicable), and upgrading the treatment planning and control systems to support the new functionality (as well as some aesthetic updates).

2.8.2 GENERAL WORKFLOW

The general IG-HSRT workflow is analogous to the Extend system in principle. An immobilization solution is created for the patient, and the patient's reference position is determined using the CBCT. A treatment plan is created using this reference CBCT as a basis for stereotactic coordinates. Prior to each treatment session, the patient is placed in the immobilization system, and a CBCT image is acquired to determine the patient's current position. The system compares the current position to the reference position and automatically corrects the treatment plan to match the current patient position. During the treatment itself, the HDMM camera system tracks the patient's motion. Treatment is automatically gated off if the patient moves out of position beyond a clinical threshold and gates back on if the patient returns to the correct position. Additional CBCT scans and corrections can be obtained if the patient does not return to the correct position within a time threshold. There are several important advantages of the Icon system over the previous Extend system, including the ease in creating a thermoplastic mask relative to a dental impression, the ease and accuracy of acquiring CBCT images to determine patient position rather than cumbersome manual distance measurements, the capability of the system to automatically adjust the treatment plan to the patient's current position rather than attempting to correct the patient's position by moving the patient, and finally the accuracy in treatment delivery gained by tracking the patient throughout the procedure and gating the delivery as required.

2.8.2.1 Setup at Gamma Knife

Setup of a patient for an IG-HSRT treatment on the Gamma Knife Icon has three primary steps: creation of a custom head-cushion, creation of a thermoplastic mask, and acquiring a reference CBCT image defining the patient's stereotactic position for treatment planning.

2.8.3 PATIENT-SPECIFIC HEAD CUSHION

The Icon system headrest is designed to accept a patient-specific head cushion. The cushions are soft while in-package but begin to harden with exposure to room air. After the patient is placed in a comfortable position on the PPS, a cushion package is opened, the cushion placed behind the patient's head and molded to fit the patient's anatomy. The cushion begins to stiffen quickly and is fully cured in approximately 15 minutes.

2.8.4 THERMOPLASTIC MASK CREATION

Thermoplastic masks have long been used in linac radiotherapy, and the mask system for the Gamma Knife Icon is quite familiar in concept. Masks arrive in packaging stiff and flat. Upon heating to approximately 165° F, the mask becomes quite deformable within 10 to 15 minutes. The heated mask is placed over the patient's face, snapped onto the appropriate locations on the headrest, and molded to match the patient's anatomy. As the mask cools it stiffens and is primary cured after approximately 15 minutes.

2.8.5 REFERENCE CBCT IMAGING

Once the patient head cushion and thermoplastic mask are created, a reference CBCT is acquired that defines the patient's reference stereotactic position. The resulting images are transferred to the treatment planning system and are co-registered to previously acquired imaging (if any). Quality of the CBCT scans is optimized for patient positioning, not for anatomical visualization, so SRS-quality MR and/or CT scans are critical for IG-HSRT treatment planning using the Icon system.

2.8.6 TREATMENT PLANNING

Treatment planning proceeds in a manner similar to G-frame-based and Extend-frame treatments. For each target, the total dose may be distributed over one or multiple fractions. A single treatment plan may include different doses, but any given treatment plan may have only one fractionation schedule. (This does not preclude treating targets with different numbers of fractions; however, separate treatment plans are required). Once treatment planning is complete, the final plan is approved and exported to the Gamma Knife Icon console.

2.8.6.1 Pre-Treatment Workflow

Pre-treatment setup of a patient involves making the patient comfortable, placing the patient in the previously created immobilization system, starting patient tracking, acquiring the patient's current stereotactic position, correcting the treatment plan to match the patient's current stereotactic position, and commencing treatment.

2.8.7 MAKING THE PATIENT COMFORTABLE AND APPLYING IMMOBILIZATION SYSTEM

The patient is placed in a comfortable position on the PPS, ideally using therapist notes on the position the patient was in during the initial setup. The patient-specific head cushion is placed behind the patient's head, and the thermoplastic mask is applied and snapped onto the patient headrest.

2.8.8 PRE-TREATMENT SETUP CBCT IMAGING

Once the patient is comfortably set up on the table, a CBCT scan is acquired in a manner similar to the images acquired for the pretreatment setup. The purpose of this image is different, however; rather than to determine a reference position for the patient, the pre-treatment CBCT determines the patient's current position. This image is exported to the treatment planning system and is co-registered relative to the reference CBCT scan via a 3-D rigid registration. The registration matrix represents the difference in stereotactic coordinate systems between the patient's reference and current positions relative to the Icon system. The treatment planning system applies this difference as a correction to the treatment plan to move it to the patient's current position. The planning system allows the operator to view the correction as well as the predicted residual dose difference after applying the correction. Once reviewed, the corrections are sent to the Gamma Knife Icon control console.

2.8.9 MOTION TRACKING AND GATING

During the pre-treatment CBCT scan, the HDMM camera system tracks the position of the patient's nose reflector relative to the four static reflectors on the headrest. A time-averaged position of the patient during the scan is computed, and this serves as a reference position for the patient's nose marker.

2.8.10 RE-IMAGING TO BASELINE PATIENT

After the corrected treatment plan is sent to the console, treatment commences. During the treatment, the HDMM system continuously tracks the patient's nose marker and allows treatment to continue as long as the magnitude of nose motion is below a clinical threshold (default is 1.5 mm, although this is user-adjustable). In the event the patient moves beyond this threshold, the control system gates the beams off by moving the sources to a blocked position. If the patient returns to a position below the threshold within 30seconds, the system will gate back on (Figure 2.15). If the patient remains out of position beyond this time limit, or if the system gates the same shot more than five times, the system will automatically pause the treatment. In this instance, a new CBCT is acquired to determine a new baseline position for the patient, a new set of corrections are generated and sent to the treatment console, and the HDMM is re-referenced.

2.8.11 IMPLICATIONS FOR WORKFLOW FLEXIBILITY

The Icon system makes a highly flexible treatment workflow possible that can accommodate multiple-dose-fractionation schemes using both thermoplastic mask and G-frame-based immobilization systems. This is supported by advances in the treatment planning system, which allow delivered dose to be accumulated and used during treatment plan design and dose evaluation. Specifically, the system includes functionality to re-plan completed cases, taking into account dose delivered in prior treatments, amend multiple-fraction treatments in-between fractions, and amend partially delivered fractions, taking into account the partial dose delivered. In each case, targets can be added/subtracted, doses can be modified, and even the immobilization system can be changed from mask to frame or vice versa. This increased flexibility enables the creation of highly personalized treatments but also requires great care and organization to ensure the treatment team has the correct information for each treatment.

2.8.12 SYSTEM ACCURACY

HSRT provides a radiobiological safety margin for the treatment of indications that would be difficult to treat in a single fraction; however, it does not eliminate the requirement for extremely low-treatment delivery uncertainties. Several studies have investigated various sources of uncertainty in the Icon CBCT and HDMM systems.

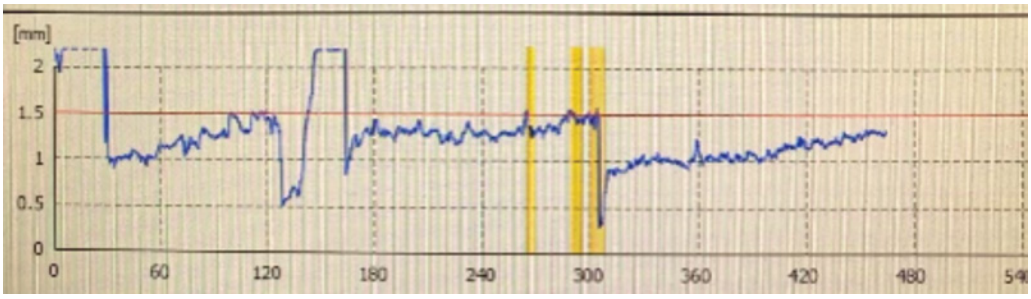

Figure 2.15 A screenshot of an HDMM trace showing the magnitude of the relative motion of the nose marker. Red line indicates the treatment gating threshold. Yellow highlights indicate times when system was gating beams because the patient was out of position beyond threshold.

2.8.12.1 Patient Motion and Gating

One of the most important sources of uncertainty for mask-based HSRT procedures on the Icon platform is the suitability of the relative motion of a reflective nose marker as a surrogate for motion of targeted anatomy. One study investigating this on both phantoms and clinical treatments found that on average, the reflective nose marker displaces about twice the magnitude of the corresponding intracranial target (Wright et al., 2019).

However, patients span a range of capacity in terms of being able to remain relatively still during treatment and tolerance of remaining in a desired position over the length of a treatment. A recent study of 462 mask patients used a neural network model to predict the probability of a treatment interruption requiring CBCT re-baselining using log-entries recorded by the HDMM system over the first 5 minutes of treatment as the model input. The analysis showed that the magnitude and frequency of nose marker motion events (relative to the most recent baseline nose position) recorded in the control system logfile could predict the occurrence of future treatment interruptions [AUC–ROC (area under the curve–receiver operating characteristics) = 0.84 for the test population]. This information could be useful during the mask creation process to determine if mask immobilization will be suitable for a given patient and could be used during the first few minutes of a treatment to measure the stability of the patient setup. The same study demonstrated that CBCT re-baselining could significantly reduce mean nose marker displacement over an entire treatment fraction (from a mean of 0.96 ± 0.96 mm to 0.62 ± 0.25 mm in the study population) (MacDonald et al., 2020).

2.8.12.2 Registration Uncertainty

Image-guided systems are critically dependent on co-registration for the calculation of the rotational and translational differences between a patient's current position with respect to the treatment machine and the position required for treatment (i.e., the treatment planning position). One study of the Icon registration system for thermoplastic mask-based immobilization cases found that the 3D image registration uncertainty as determined by anterior commissure/posterior commissure landmarks was on the order of 0.2 mm when co-registering CBCT to CBCT images, 0.5 mm when co-registering CT to CBCT images, and 0.8 mm when co-registering MR to CBCT images, with best results obtained when including the skull base in the registration region-of-interest (Chung et al., 2018).

2.8.12.3 Quality Assurance of Frame-Based Cases

While the Icon system was optimized for using thermoplastic mask immobilization, the Icon CBCT system offers important benefits for quality assurance for G-frame-based treatments. Because the CBCT images are natively acquired in stereotactic space, they can be used as an independent check for G-frame-based treatment plans where stereotactic coordinates are defined using an indicator box that mounts to the frame system itself. These two stereotactic coordinate systems should nominally be identical. In practice, there are uncertainties in each measurement, which can be estimated by acquiring a pre-treatment CBCT of a G-frame patient and co-registering the CBCT images to the frame/fiducial images used for treatment planning. The co-registration differences represent the difference between the independent stereotactic coordinate systems. Problems such as mis-applied indicator boxes at the time of imaging or more seriously a shift in the frame between treatment planning imaging and the CBCT will become apparent as an unusually large co-registration error. Studies using the CBCT system in this way have demonstrated that G-frames have an expectedly low setup uncertainty, with mean residual uncertainties after setup reported to be on the order of 0.3 mm in translation on each orthogonal axis and rotations below 0.5 degrees around each axis (Dutta et al., 2018). Rarely, a larger frame shift may occur due to errors in pin placement, pin length, and head size. The CBCT system makes these shifts simple to detect and correct before a procedure commences (Peach et al., 2018). CBCT verification of frame stability may be especially helpful in situations where a frame has been placed using only three of the four posts (Stieler et al., 2018).

2.8.13 LIMITATIONS OF THE GAMMA KNIFE ICON

The Icon system represents a significant improvement in support for IG-HSRT procedures on the Gamma Knife platform. However, it is not without some limitation.

2.8.13.1 Support for Multiple Single-Fraction Workflows

One common workflow used with mask-based treatments is to treat multiple small lesions in a patient using multiple single-fraction procedures. The use of thermoplastic masks makes this workflow practical to accomplish; however, at present the treatment planning system provides no way to create a comprehensive treatment plan and simply select which targets to treat on which treatment sessions. Instead, individual treatments must be replanned manually and the total dose evaluated by accumulating dose as treatments progress.

2.8.13.2 Radiobiological Effects

The dose accumulation functionality of the treatment planning system calculates total dose by simple dose addition, not through the use of any radiobiological model. This brings up the question of how to manage various multi-session and reirradiation scenarios (Sanders et al., 2019).

2.8.13.3 The Future of Gamma Knife IG-HSRT: Advances in Treatment Planning with Gamma Knife Lightning

Gamma Knife treatment planning has historically utilized a forward-planning technique. The individual operating the treatment planning software was responsible for manually placing isocenters, in the process determining the number and collimator sizes of isocenters, relative isocenter weighting, and prescription isodose lines. Practical treatment tradeoffs such as acceptable conformity and dose falloff versus treatment time were left up to the individual.

The development of the Icon platform and the ability for performing IG-HSRT procedures using a flexible workflow makes the idea of adaptive radiosurgery treatments practical. More frequent treatment planning in turn would benefit from a more automated and consistent treatment planning paradigm. While recent versions of the Gamma Knife treatment planning system have included functionality to automatically place isocenters and then optimize treatments against dose metrics such as conformity, selectivity, and beam-time (Schlesinger et al., 2010), the system has not included a complete inverse-planning solution based on dose–volume constraints and objectives.

There have been several historical attempts to create these kind of fully functional inverse treatment planning solutions for GKRS (Shepard et al., 2000; Wu et al., 2003; Ghobadi et al., 2012; Tian et al., 2020; Xu et al., 2020); however, these have not been commercially adopted (with few exceptions [Levivier et al., 2018]). Elekta Instrument, AB, recently (at the time of this publication) announced the availability of Gamma Plan Lightning, which includes this functionality. The new treatment planning algorithm proceeds through three steps. The first step is isocenter placement, which is dependent on contouring the intended target. Once isocenters are placed, they remain fixed. After isocenter placement, an optimization algorithm based on a linear programming model attempts to find a solution that best meets various dose/volume and other treatment planning objectives and constraints by optimizing individual sector durations. Finally, a shot-sequencing step recombines these individually optimized sector durations into deliverable shots. Importantly, the algorithm can include practical treatment considerations such as beam-on-time into the optimization as well as more traditional dose/volume objectives/constraints. Early tests of the algorithm report fast (median time 5.7 seconds) optimization times, equal or better treatment planning metrics, and a factor of 2–3 reduction in beam-on-time as compared to traditional forward plans on the current generation of computer hardware distributed by the manufacturer (Sjolund et al., 2019). The lightening system will also include improvements in contouring, an ability to determine the order in which multiple targets are treated, as well as back-end improvements for functions such as backup and recovery.

2.9 CONCLUSIONS

Radiosurgery has evolved remarkably as compared to previous decades, led by advances in existing surgical-delivery platforms including the Gamma Knife platform. Radiosurgery has become more flexible, expanding from a strictly single-fraction modality to encompassing a variety of multi-fraction treatment strategies. The Gamma Knife platform has evolved to take advantage of technologies that make this flexibility possible without sacrificing the precision and accuracy that have established Gamma Knife as the "gold standard" for radiosurgery. Future improvements may focus on radiobiological considerations that will allow further customization of Gamma Knife IG-HSRT and truly personalized radiosurgical care.

REFERENCES

AlDahlawi I, Prasad D, Podgorsak MB (2017) Evaluation of stability of stereotactic space defined by cone-beam CT for the Leksell Gamma Knife icon. *Journal of Applied Clinical Medical Physics* 18:67–72.

Alheit H et al. (1999) Stereotactically guided conformal radiotherapy for meningiomas. *Radiotherapy and Oncology: Journal of the European Society for Therapeutic Radiology and Oncology* 50:145–150.

Baumert BG, Egli P, Studer S, Dehing C, Davis JB (2005) Repositioning accuracy of fractionated stereotactic irradiation: Assessment of isocentre alignment for different dental fixations by using sequential CT scanning. *Radiotherapy and Oncology: Journal of the European Society for Therapeutic Radiology and Oncology* 74:61–66.

Casentini L, Fornezza U, Perini Z, Perissinotto E, Colombo F (2015) Multisession stereotactic radiosurgery for large vestibular schwannomas. *Journal of Neurosurgery*: 1–7.

Chung HT et al. (2018) Assessment of image co-registration accuracy for frameless Gamma Knife surgery. *PloS One* 13:e0193809.

Davey P, Schwartz M, Scora D, Gardner S, O'Brien PF (2007) Fractionated (split dose) radiosurgery in patients with recurrent brain metastases: Implications for survival. *British Journal of Neurosurgery* 21:491–495.

Dong L, Shiu A, Tung S, Boyer A (1997) Verification of radiosurgery target point alignment with an electronic portal imaging device (EPID). *Medical Physics* 24:263–267.

Dutta SW et al. (2018) Stereotactic shifts during frame-based image-guided stereotactic radiosurgery: Clinical measurements. *International Journal of Radiation Oncology, Biology, Physics* 102:895–902.

Eriksson M, Nordström H (2014) Design and performance characteristics of a cone beam CT system for the LGK perfexion. In: *17th International Leksell Gamma Knife Society Meeting*. New York, NY.

Eriksson M, Nutti B, Hennix M, Malmberg A, Nordström H (2014) Position accuracy analysis of the stereotactic reference defined by CBCT on LGK perfexion. In: *17th International Leksell Gamma Knife Society Meeting*. New York, NY.

Ghobadi K, Ghaffari H, Aleman D, Ruschin M, Jaffray D (2012) SU-D-211–03: An Automated inverse planning optimization approach for single-fraction and fractionated radiosurgery using Gamma Knife perfexion. *Medical Physics* 39:3610.

Jaffray DA (2007) Kilovoltage volumetric imaging in the treatment room. *Frontiers of Radiation Therapy and Oncology* 40:116–131.

Jee TK et al. (2014) Fractionated Gamma Knife radiosurgery for benign perioptic tumors: Outcomes of 38 patients in a single institute. *Brain Tumor Research and Treatment* 2:56–61.

Kirchheiner K et al. (2014) Posttraumatic stress disorder after high-dose-rate brachytherapy for cervical cancer with 2 fractions in 1 application under spinal/epidural anesthesia: Incidence and risk factors. *International Journal of Radiation Oncology, Biology, Physics* 89:260–267.

Kunieda E et al. (2009) The reproducibility of a HeadFix relocatable fixation system: Analysis using the stereotactic coordinates of bilateral incus and the top of the crista galli obtained from a serial CT scan. *Physics in Medicine and Biology* 54:N197–204.

Leksell Gamma Knife Society (2019) Leksell Gamma Knife: Indications treated 1968–2019. In: (Society LGK, ed).

Leksell L (1951) The stereotaxic method and radiosurgery of the brain. *Acta Chirurgica Scandinavica* 102:316–319.

Levivier M, Carrillo RE, Charrier R, Martin A, Thiran JP (2018) A real-time optimal inverse planning for Gamma Knife radiosurgery by convex optimization: Description of the system and first dosimetry data. *Journal of Neurosurgery* 129:111–117.

Lindquist C, Paddick I (2007) The Leksell Gamma Knife Perfexion and comparisons with its predecessors. *Neurosurgery* 61:130–140; discussion 140–131.

Lunsford LD, Flickinger JC, Steiner L (1988) The Gamma Knife. *JAMA* 259:2544.

Ma L, Pinnaduwage D, McDermott M, Sneed PK (2014) Whole-procedural radiological accuracy for delivering multi-session Gamma Knife radiosurgery with a relocatable frame system. *Technology in Cancer Research & Treatment* 13:403–408.

MacDonald RL, Lee Y, Schasfoort J, Soliman H, Sahgal A, Ruschin M (2020) Real-time infrared motion tracking analysis for patients treated with gated frameless image guided stereotactic radiosurgery. *International Journal of Radiation Oncology, Biology, Physics* 106:413–421.

Minniti G et al. (2010) Fractionated stereotactic radiotherapy for skull base tumors: Analysis of treatment accuracy using a stereotactic mask fixation system. *Radiation Oncology* (London, England) 5:1.

Minniti G et al. (2014) Fractionated stereotactic radiosurgery for patients with skull base metastases from systemic cancer involving the anterior visual pathway. *Radiation Oncology* (London, England) 9:110.

Peach MS, Trifiletti DM, Dutta SW, Larner JM, Schlesinger DJ, Sheehan JP (2018) Spatial shifts in frame-based Gamma Knife radiosurgery: A case for cone beam CT imaging as quality assurance using the Gamma Knife(R) Icon. *Journal of Radiosurgery and SBRT* 5:315–322.

Pouliot J et al. (2005) Low-dose megavoltage cone-beam CT for radiation therapy. *International Journal of Radiation Oncology, Biology, Physics* 61:552–560.
Reisberg DJ, Shaker KT, Hamilton RJ, Sweeney P (1998) An intraoral positioning appliance for stereotactic radiotherapy. *The Journal of Prosthetic Dentistry* 79:226–228.
Rosenberg I, Alheit H, Beardmore C, Lee KS, Warrington AP, Brada M (1999) Patient position reproducibility in fractionated stereotactic radiotherapy: An update after changing dental impression material. *Radiotherapy and Oncology: Journal of the European Society for Therapeutic Radiology and Oncology* 50:239–240.
Ruschin M et al. (2013) Cone beam computed tomography image guidance system for a dedicated intracranial radiosurgery treatment unit. *International Journal of Radiation Oncology, Biology, Physics* 85:243–250.
Ruschin M et al. (2010) Performance of a novel repositioning head frame for Gamma Knife perfexion and image-guided linac-based intracranial stereotactic radiotherapy. *International Journal of Radiation Oncology, Biology, Physics* 78:306–313.
Ryken TC et al. (2001) Initial clinical experience with frameless stereotactic radiosurgery: Analysis of accuracy and feasibility. *International Journal of Radiation Oncology, Biology, Physics* 51:1152–1158.
Salter BJ et al. (2001) The TALON removable head frame system for stereotactic radiosurgery/radiotherapy: Measurement of the repositioning accuracy. *International Journal of Radiation Oncology, Biology, Physics* 51:555–562.
Sanders J, Nordstrom H, Sheehan J, Schlesinger D (2019) Gamma Knife radiosurgery: Scenarios and support for re-irradiation. *Physica Medica: PM: An International Journal Devoted to the Applications of Physics to Medicine and Biology: Official Journal of the Italian Association of Biomedical Physics* 68:75–82.
Sayer FT, Sherman JH, Yen CP, Schlesinger DJ, Kersh R, Sheehan JP (2011) Initial experience with the eXtend System: A relocatable frame system for multiple-session Gamma Knife radiosurgery. *World Neurosurgery* 75:665–672.
Schlesinger D, Xu Z, Taylor F, Yen CP, Sheehan J (2012) Interfraction and intrafraction performance of the Gamma Knife Extend system for patient positioning and immobilization. *Journal of Neurosurgery* 117(Suppl):217–224.
Schlesinger DJ, Sayer FT, Yen CP, Sheehan JP (2010) Leksell GammaPlan version 10.0 preview: Performance of the new inverse treatment planning algorithm applied to Gamma Knife surgery for pituitary adenoma. *Journal of Neurosurgery* 113(Suppl):144–148.
Shepard DM, Ferris MC, Ove R, Ma L (2000) Inverse treatment planning for Gamma Knife radiosurgery. *Medical Physics* 27:2748–2756.
Simonova G, Novotny J, Novotny J, Jr., Vladyka V, Liscak R (1995) Fractionated stereotactic radiotherapy with the Leksell Gamma Knife: Feasibility study. *Radiotherapy and Oncology: Journal of the European Society for Therapeutic Radiology and Oncology* 37:108–116.
Sjolund J, Riad S, Hennix M, Nordstrom H (2019) A linear programming approach to inverse planning in Gamma Knife radiosurgery. *Medical Physics* 46:1533–1544.
Stieler F, Wenz F, Schweizer B, Polednik M, Giordano FA, Mai S (2018) Validation of frame-based positioning accuracy with cone-beam computed tomography in Gamma Knife Icon radiosurgery. *Physica Medica: PM: An International Journal Devoted to the Applications of Physics to Medicine and Biology: Official Journal of the Italian Association of Biomedical Physics* 52:93–97.
Sweeney R et al. (1998) Repositioning accuracy: Comparison of a noninvasive head holder with thermoplastic mask for fractionated radiotherapy and a case report. *International Journal of Radiation Oncology, Biology, Physics* 41:475–483.
Tian Z et al. (2020) A preliminary study on a multiresolution-level inverse planning approach for Gamma Knife radiosurgery. *Medical Physics* 47:1523–1532.
Toma-Dasu I, Sandstrom H, Barsoum P, Dasu A (2014) To fractionate or not to fractionate? That is the question for the radiosurgery of hypoxic tumors. *Journal of Neurosurgery* 121(Suppl):110–115.
Treuer H et al. (2006) Impact of target point deviations on control and complication probabilities in stereotactic radiosurgery of AVMs and metastases. *Radiotherapy and Oncology: Journal of the European Society for Therapeutic Radiology and Oncology* 81:25–32.
Viola P, Wells III WM (1997) Alignment by maximization of mutual information. *International Journal of Computer Vision* 24:137–154.
Wright G, Harrold N, Hatfield P, Bownes P (2017) Validity of the use of nose tip motion as a surrogate for intracranial motion in mask-fixated frameless Gamma Knife Icon therapy. *Journal of Radiosurgery and SBRT* 4:289–301.
Wright G, Schasfoort J, Harrold N, Hatfield P, Bownes P (2019) Intra-fraction motion gating during frameless Gamma Knife Icon therapy: The relationship between cone beam CT assessed intracranial anatomy displacement and infrared-tracked nose marker displacement. *Journal of Radiosurgery and SBRT* 6:67–76.
Wu QJ et al. (2003) Real-time inverse planning for Gamma Knife radiosurgery. *Medical Physics* 30:2988–2995.
Xu Q et al. (2020) Tuning-target-guided inverse planning of brain tumors with abutting organs at risk during Gamma Knife stereotactic radiosurgery. *Cureus* 12:e9585.

3 CyberKnife Image-Guided Hypofractionated Stereotactic Radiotherapy

Christopher McGuinness, Martina Descovich and Cynthia Chuang

Contents

3.1 HISTORICAL OVERVIEW OF THE CYBERKNIFE SYSTEM

The CyberKnife system is a fully integrated platform for stereotactic radiosurgery (SRS) and stereotactic body radiation therapy (SBRT) treatments. The delivery system consists of a linear accelerator (Linac) mounted on a robotic arm enabling the delivery of radiation from hundreds of noncoplanar, nonisocentric beams around the patient. Stereotactic targeting accuracy is achieved by combining real-time orthogonal x-ray images with advanced image recognition software for automatic tracking of bony landmarks, implanted fiducials, or clearly distinguishable tumors within the lung. This allows the delivery of highly conformal hypofractionated treatments in the entire body without the need for rigid fixation devices. Figure 3.1 shows a CyberKnife treatment vault with the important components labeled.

The CyberKnife system came to market in the late 1990s. The first prototype was installed at Stanford University. It was designed as a frameless alternative to the existing SRS systems for the treatment of brain and C spine lesions. The CyberKnife prototype was called Neutroton 1000. Since the initial design, Accuray Inc. (Sunnyvale, CA) released five CyberKnife models: the G3 system in 2002, the G4 system in 2005, the VSI system in 2009, the M6 system in 2012, and the S7 system in 2020.

Over the years, the development of new tracking methods (including fiducial-free spine and lung tracking) and the capability to track respiratory motion in real time allowed to expand the clinical applications of CyberKnife to several extracranial sites including the spine, lung, liver, pancreas, and prostate (Kilby et al., 2010). Further improvements in the beam collimator and delivery system resulted in a considerably faster treatment time and making it possible to treat larger lesions. Notably, the major change introduced by the M6™ system was the addition of the InCise™ micro-multileaf collimator (MLC) to the collimator system. The addition of the MLC has been shown to significantly reduce treatment time by 30% to 50% while maintaining or improving treatment quality (McGuinness et al., 2015; Kim et al., 2017).

Hardware improvements have been matched by advances in the treatment planning system (TPS). Multiplan® replaced the original On Target® in 2005, providing advanced dose optimization algorithms and beam/time reduction techniques (Schlaefer et al., 2008), Monte Carlo dose calculation (Ma et al., 2008), automatic segmentation, and deformable image registration. In 2017, the Precision® treatment planning system was released, which included the Volo™ optimizer. This new TPS and optimization algorithm significantly reduced the amount of time required for developing treatment plans while improving the quality and efficiency of the treatments delivered (Schüler et al., 2020).

3.1.1 SYSTEM SPECIFICATIONS

The CyberKnife system consists of an X-band cavity magnetron and a side-coupled standing wave LINAC mounted on a robotic manipulator (Kuka Roboter GmbH, Augsburg, Germany). The linac produces an unflattened 6 MV photon beam with a dose rate up to 1000 cGy/min. The beam is collimated using one of three collimator systems: (1) the fixed collimator assembly (FCA), (2) the Iris™ variable aperture collimator, and (3) the InCise™ micro-multileaf collimator (MLC). The FCA consists of 12 circular tungsten cones with diameters ranging from 5 to 60 mm. Field size is defined at a source-to-axis distance (SAD) of 800 mm. The Iris collimation system consists of two hexagonal banks of tungsten, producing a 12-sided aperture, with the same set of field sizes available as the FCA (Echner et al., 2009). The mechanical uncertainty of the Iris field sizes is 0.2 mm, which affects the output factor for the smallest field size (5, 7.5, and 10 mm). The uncertainty in output factor for the 5 mm aperture can be up to 10% and is approximately 1.4% for the 10 mm aperture. While the manufacturer restricts the use of the 5 mm aperture, we do not recommend using either 5 or 7.5 mm Iris aperture for clinical cases.

Plans generated with multiple apertures typically result in better quality (dose conformity and gradient) and require a lower number of monitor units (MUs) (Pöll et al., 2008). However, using multiple fixed cones is not practical because it requires multiple path traversals and results in excessively long treatment times.

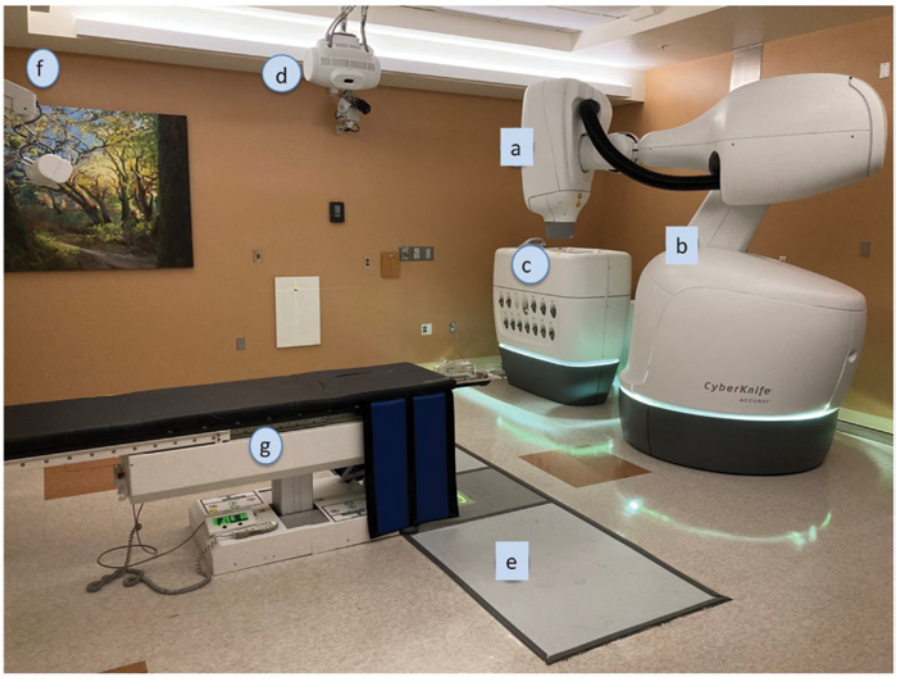

Figure 3.1 Image of a CyberKnife treatment suite. (a) Linear accelerator. (b) Robotic manipulator arm. (c) Exchange table with the fixed collimator assembly, the Iris™ variable aperture collimator, and the InCise™ micro-multileaf collimator. (d) X-ray imaging source. (e) Flat-panel detector. (f) Synchrony® camera array. (g) Patient positioning couch.

The Iris collimator allows using multiple apertures without these limitations. To further improve the delivery efficiency, the Incise MLC collimator was introduced in 2014, followed by an updated model in 2015. The first MLC model consists of 41 pairs of tungsten leaves with a width of 2.5 mm allowing a maximum field size of 120 mm (leaf motion direction) by 102.5 mm at 800 mm SAD. The second MLC model consists of 26 pairs of leaves with a width of 3.85 mm allowing a maximum field size of 115 mm by 100.1 mm. The leaves are interdigitated and can reach fully over-traveled positions. The leaf's height is 90 mm, and the maximum interleaf leakage is less than 0.5% (Accuray Inc., 2018). The addition of the micro-MLC has been shown to reduce MU and treatment time by 30% to 50% with equivalent or improved conformality, dose gradient, and critical organ sparing (Van De Water et al., 2011; McGuinness et al., 2015). Kim et. al. published a comparison of 144 cases of spine SBRT treatments where 78 were treated with fixed collimators, and 66 were treated with MLC collimator. They demonstrated a reduction in dose gradient and treatment times by 30% for the MLC cases while maintaining equivalent or improved dose coverage, conformity, and local recurrence rates between the two groups (Kim et al., 2017).

An automated exchange table system enables switching between the collimator housing. For early CyberKnife models, the exchange table contains receptacle storage spaces for the Iris housing, the FCA, and the 12-fixed tungsten cones and enables changing the cones automatically during treatment. For the M6 and S7 models, the exchange table contains the additional storage space for the MLC assembly. However, due to space limitation on the exchange table, the automatic exchange of the 12-fixed cones is no longer available.

Treatments are delivered from hundreds of beams arranged around the target. Each beam is defined by a source point, called a node, a direction, and a field size. Plans with the micro-MLCs may have several segments with different MLC leaf patterns for each beam. The complete set of nodes is called the path set and contains a different number of positions depending on the collimator type and treatment site. For the fixed and Iris collimator, the head path contains 179 nodes and the body path contains 117 nodes. For the MLC, the head path contains 171 nodes and the body path contains 102 nodes. The MLC path sets have fewer nodes to accommodate the slightly larger MLC housing.

The image-guided system consists of two diagnostic x-ray sources mounted in the ceiling and two amorphous silicon flat-panel detectors embedded in the floor, imaging the patient from two orthogonal oblique views at ±45°. Target localization during patient setup and treatment delivery is achieved by comparing the live x-ray images with a library of digitally reconstructed radiographs (DRRs) pre-generated from the planning CT at 45° angles through the imaging center. Based on this comparison, the tracking software calculates the differences in the three translational and three rotational directions between simulation and treatment positions as the couch correction parameters. Patients are positioned on a motorized treatment table with either five or six degrees of freedom, depending on the couch model. If the couch correction parameters are below the threshold set for treatment, the robot retargets the radiation beams, without the need to stop the treatment to move the patient couch.

The CyberKnife system includes an integrated treatment planning system allowing a fully autonomous environment for image fusion, contouring, DRR generation, treatment planning, plan evaluation, and patient-specific QA generation. In 2017, a new TPS, Precision, was released (Accuray, Inc.). It offers the same capabilities as the previous system (Multiplan) but with several improvements such as the new optimization algorithm, Volo, which reduces optimization time and improves plan quality (Schüler et al., 2020; Zeverino et al., 2019).

3.2 PATIENT SETUP AND TREATMENT SIMULATION

Proper patient setup and simulation is important for ensuring the full capabilities of the system during treatment planning and delivery. It is particularly important to ensure the patient is comfortable at the time of simulation so they can maintain the same position over the course of a 20- to 60-minute treatment. For brain lesions, a thermoplastic head mask with a headrest should be used. For cervical spine lesions, a head and shoulder mask should be used to minimize motion of the head and neck. For thoracic or lumbar spine lesions, a vacuum bag or foam cradle can be used to immobilize the thoracic, abdominal, or pelvic regions. Alternatively, patients can be positioned just on a foam pad to improve comfort, as patients positioned comfortably are less likely to move during treatment. For thoracic cases, the patient can be placed on a thick pad so their arms fall below the level of the body, thereby increasing the potential number

of lateral beams that can be used without concern for beams passing through the arms. This is preferred instead of raising the arms overhead for two reasons: (1) to prevent the arms extending outside of the patient safety zone, which could potentially cause collision; (2) the position of arms overhead could be difficult and tiring for patients to maintain for the whole treatment duration. For lumbar and pelvic cases, the arms can rest on the patient's chest.

CT simulation is usually performed with the patient in the supine position. A CT scan with slice thickness between 1 and 1.5 mm is recommended. The slice thickness is important as finer slices result in higher-resolution DRRs and ultimately result in better tracking accuracy (Adler et al., 1999). The scan should be centered on the target extending 10 to 15 cm above and below the superior and inferior border of the target and/or encompassing all the organs at risk (OAR) such as lungs, bowels, stomach, or liver. This may be a longer scan than is typical for linac-based treatments because the noncoplanar beam arrangement in CyberKnife requires the scan to include any region along the patient anatomy where a potential beam will enter. The primary CT used for treatment planning must be a noncontrast CT as the contrast-enhancing agents might distort the quality of the DRR and impact tracking accuracy.

3.3 VOLUME DEFINITION AND TREATMENT PLANNING

A CT image is required for dose calculation during treatment planning and to generate DRRs used for patient setup and tracking during treatment delivery. Other imaging modalities such as MRI, PET, or additional CT scans can be incorporated directly in the TPS and registered to the primary CT image. Image registration and fusion can be performed manually or semiautomatically using fiducial marker positions or maximization of mutual information (Maurer and West, 2006). In the Precision TPS, a fast multi-modal method for deformable image registration (DIR) is also available (P Jordan et al., Accuray deformable image registration: description and evaluation, Accuray White Paper), enabling fast autosegmentation of cranial and head and neck anatomy. The autosegmentation tool is based on an atlas-based approach. Due to the variability of cranial anatomy, the system matches the patient image with multiple atlas images and chooses one optimal CT and three optimal MR atlas images. It uses a nonrigid registration algorithm to map the atlas image onto the patient's CT and T1-weighted MR image (Studholme et al., 1996). A set of warped contours is generated for the patient image from the set of atlas contours following the registration process.

The MR images are fused onto CT images for contouring, treatment planning, and evaluation. Brain lesions are contoured using gadolinium-enhanced T1-weighted Magnetization Prepared—RApid Gradient Echo (MPARAGE) or similar sequences and T2-weighted fluid-attenuated inversion recovery (FLAIR) MRI sequences. Primary brain tumor lesions, postoperative resection cavities, single and multiple brain metastasis, and benign diseases (such as trigeminal neuralgia or arteriovenous malformation) can be treated on the CyberKnife. Ma et al. evaluated the relationship of number of targets and radiosurgery platform with the dose to normal brain (Ma et al., 2011a) and developed an optimization technique to improve the planning quality of multiple metastasis treatments (Ma et al., 2011b). Small lesions are typically treated in a single fraction as in Gamma Knife radiosurgery. Larger lesions, or lesion located in critical areas (near the optic structures or the brainstem), are treated in 3–5 fractions. The high conformality and steep dose gradient for a case with multiple brain metastases can be seen in Figure 3.2. Brain metastases are usually treated with small planning target volume (PTV) margin (0–1 mm). For postoperative brain cases, the surgical resection cavity is usually expanded by 2 mm to create the clinical target volume (CTV)/PTV (Murphy, 2009).

Target volume definition for spinal SBRT is described in Radiation Therapy Oncology Group (RTOG) 0631 (Ryu, 2011) and in a consensus report (Cox et al., 2012). To summarize, MR and CT images are fused to help define the target volume and spinal cord. The CTV should encompass any abnormal marrow signal and adjacent normal bone. Single and multilevel spinal lesions can be treated with the CyberKnife. Figure 3.3 shows an example of dose distribution for a single thoracic spine lesion. A highly conformal dose distribution can be achieved with sharp dose falloff near the spinal cord. Notably, even the low-dose isodose line (i.e., 5 Gy) bends away from the spinal cord. Sahgal et al. developed a treatment planning approach to improve the dose distribution in multiple consecutive vertebral body metastases (Sahgal et al.,

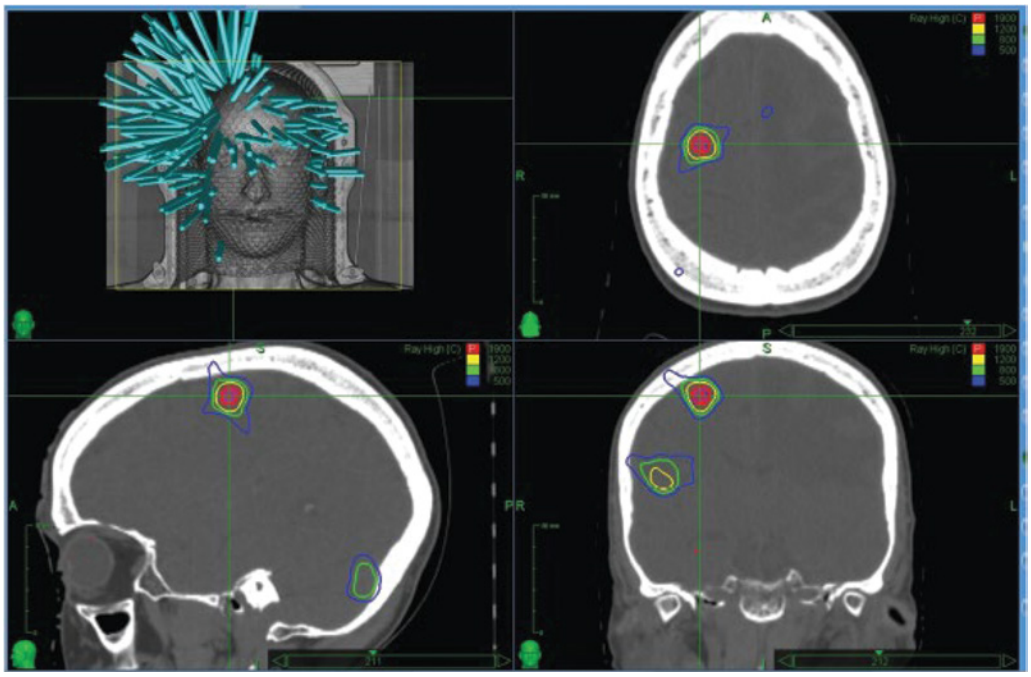

Figure 3.2 An example of a plan with three separate brain metastases. The prescription dose for this case was 19 Gy as shown in red. The 5 Gy isodose is shown in blue.

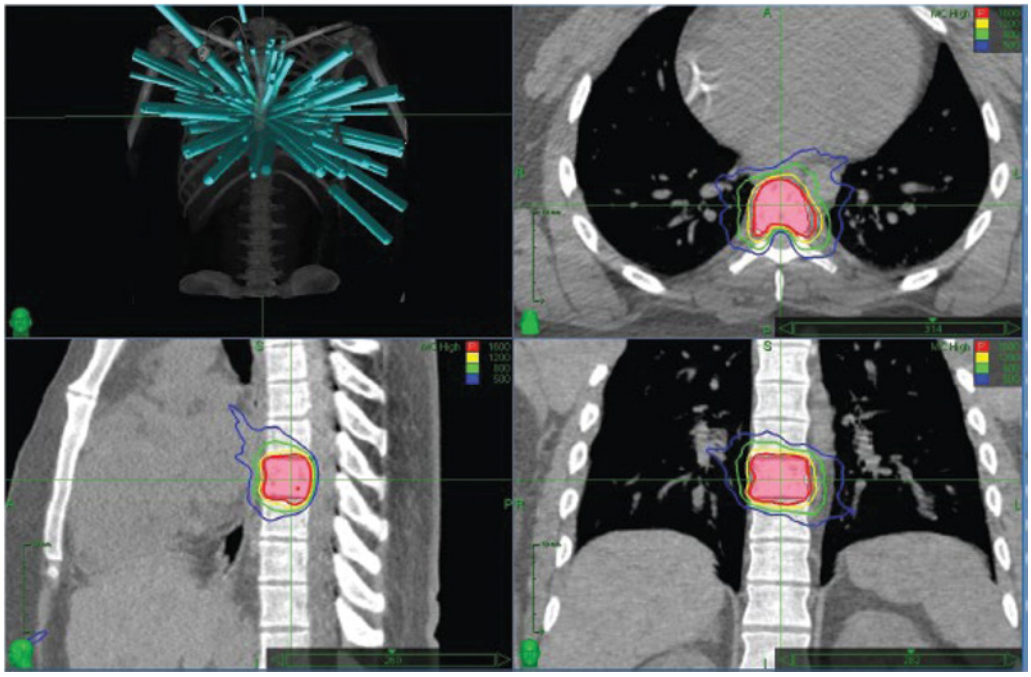

Figure 3.3 The dose distribution for this thoracic spine lesion demonstrates the conformality and sharp dose fall-off near the spinal cord that can be achieved with a large number of noncoplanar beams available on CyberKnife. The prescription isodose for this case was 16 Gy shown in red. The 8 and 5 Gy isodose levels are shown in green and blue, respectively.

2008). The spinal cord must be taken into special consideration for these treatments. Often a 2-mm expansion is included on the contoured spinal cord volume, and the expanded volume is subtracted from the PTV adding a safety margin to compensate for contouring and registration uncertainties and possible misalignment during treatment. Chuang et al. investigated the effects of residual target motion in CyberKnife radiosurgery and calculated patient-specific residual target motions on the order of 2 mm (Chuang et al., 2007). Fürweger et al. (2010) evaluated the targeting accuracy and residual motion in 260 patients treated with single-fraction CyberKnife radiosurgery and concluded that submillimeter targeting accuracy could be achieved despite patient motion. In a more recent study, Pantelis et al. (2018) reported the total geometric treatment uncertainty of a CyberKnife system using phantom-based and patient-based methods. The clinical targeting accuracy was estimated by analyzing treatment and follow-up data of a patient treated for a thalamic functional lesion. All their measurements demonstrated a total system uncertainty less than 1 mm for fiducial tracking, Xsight spine tracking, and 6D skull tracking methods.

3.4 PLAN OPTIMIZATION AND DOSE CALCULATION

CyberKnife can deliver both isocentric and non-isocentric plans. In isocentric plans, all the beams are directed to a single point in space, called treatment isocenter. Isocentric plans are adequate only for small spherical targets and have limited applications. The majority of treatments are delivered via non-isocentric beams directed to the periphery of the target. In Precision® TPS, non-isocentric plans can be generated using two optimization methods: Sequential and Volo.

The Sequential optimization algorithm proposed by Schlaefer and Schweikard (2008) was developed in early versions of Multiplan® TPS to mimic the decision-making process of a clinician. The optimization problem is framed, given thousands of possible beams defined by node position, beam angle, and collimator size (for fixed or Iris plans) or segment shape (for MLC plans). Once the beam parameters are chosen, the user can define dose–volume constraints and objectives, and the optimization algorithm finds the best subset of beams and beam weights to meet them. However, rather than setting weights to prioritize importance (as in simplex or iterative optimization algorithms), the objectives are defined in the order of decreasing importance. The optimizer manipulates beams and beam weights until the first objective is met and then proceeds to the next objectives sequentially. The solution for each prior step becomes a constraint with a user-defined relaxation factor as the optimizer moves to subsequent objectives. In this way, target coverage can be guaranteed before minimizing dose to OAR. While Sequential optimization works well for relatively simple cases, it has some limitations. In particular, for MLC plans the optimization process requires the generation of predefined segment shapes, resulting in long optimization times. In order to improve the optimization speed and to incorporate delivery efficiency in the optimization problem, the Volo optimizer was developed. In the Volo optimizer, the dose–volume goals, their importance (weighting), and the delivery efficiency objectives are all combined in a single cost function. For MLC plans, a fluence-based optimization step is followed by segmentation and aperture adaptation. It has been shown that plans optimized with Volo have superior dosimetric characteristics, are more efficient, and can be delivered in less time, compared to plan generated with the Sequential optimizer (Schüler et al, 2020).

Two dose calculation algorithms are available: ray tracing and Monte Carlo. The ray-tracing algorithm accounts for heterogeneity corrections along the primary path only. It computes an effective path length based on the electron density in the CT image but does not include effects of tissue inhomogeneity on scattered radiation. A contour correction is applied to the ray-tracing algorithm to estimate the effective depth of off-axis points. The beam for a given collimator size is divided into 12 equally spaced rays at 30° intervals around the perimeter of the cone, which are calculated using a trilinear interpolation with the nearest four rays. Contour correction improves the accuracy of dose calculation for oblique beam incidence and should be selected in the case of superficial targets.

The Monte Carlo algorithm includes the effect of tissue inhomogeneity on the scattered dose, which can be quite significant at air–tissue interfaces and somewhat significant at bone–tissue interfaces. Differences in dose calculations can be quite significant in lung cases when planning with ray tracing versus Monte Carlo algorithm (Wilcox et al., 2010). It is recommended to use Monte Carlo for final dose calculation in all thoracic cases and for targets near the sinuses or other air cavities.

3.5 TREATMENT DELIVERY AND IMAGE GUIDANCE

The CyberKnife system is capable of delivering highly conformal dose distributions with stereotactic imaging accuracy making it well suited for hypofractionated treatments. To ensure the conformal dose distribution is being delivered to the desired target volume while sparing adjacent OAR, highly accurate target localization and real-time tracking capabilities are implemented using sophisticated image guidance. A pair of orthogonal kilovoltage x-ray sources and detectors provides high contrast images of bony landmarks or fiducial markers which can be used for patient setup and accurate motion tracking in real time throughout the treatment. Images can be taken every 15 to 150 seconds (typical imaging frequency is 30 to 60 seconds, depending on treatment site).

3.5.1 FIDUCIAL TRACKING

Fiducial tracking uses radio-opaque markers for positioning. Ideally, three or more separate markers with adequate distance apart should be used to provide 6D corrections (three translations and three rotations). This is most commonly used for prostate and liver lesions where fiducial markers are implanted directly into the organ. It can also be used for lung cases though risk of pneumothorax due to fiducial implantation must be considered for this approach. There is a fiducial-free option for tracking lung lesions that can be clearly distinguished on orthogonal x-ray images. Screws or pins fixed to the vertebral body can also be used for fiducial tracking though this is rare as other fiducial-less tracking methods have been developed for spine lesions.

3.5.2 6D SKULL TRACKING

Skull tracking is used for intracranial cases or for any site that is considered fixed with respect to the skull. The patient's skull is imaged with 2D orthogonal images, and a transformation algorithm determines the best linear transformation between the image and the DRR. The transformations are combined and back projected to determine the 6D transformation that best aligns the current skull position to the original planning CT skull position. The algorithm is described by Fu and Kuduvalli (2008).

3.5.3 XSIGHT SPINE TRACKING

Xsight spine tracking is used for spine lesions—cervical, thoracic, lumbar, and sacral—or for any sites that are considered fixed with respect to the spine. Image registration is based on the differential contrast between bony features in the vertebral bodies. During planning, the user defines an imaging center that is just anterior to the spinal cord and midline relative to the vertebral body. A grid of 81 (9 × 9) nodes, shown in Figure 3.4, is displayed over each of the two orthogonal DRRs, usually encompassing several vertebral bodies. The user can adjust the overall size of the grid to maximize the number of nodes containing bony features. It is best to place the middle node (imaging isocenter) at a location with higher bony density in the DRR to ensure the algorithm's capability to calculate rotations consistently. A box matching algorithm computes local displacement vectors for each node point between the image taken of the patient during treatment and the original DRR and computes a final translation and rotation vector used to register the patient (Fu et al., 2006). The algorithm has been demonstrated to be very robust with a total system accuracy of 0.61 mm (Ho et al., 2007).

3.5.4 XSIGHT SPINE TRACKING IN THE PRONE POSITION

Spinal treatments delivered in the prone position can benefit from decreased dose given to anterior organs such as the heart and bowels (Descovich et al., 2012). This is due to the increased number of beams available from posterior directions that are unavailable when the patient is positioned supine due to physical limitation of the robot and couch. However, breathing motion becomes a significant problem for spine treatments when the patient is prone (Fürweger et al., 2011). Even if breathing motion is compensated, a 2-mm margin should be added to the CTV to account for the reduced accuracy of respiration-compensated tracking. This additional margin may reduce the potential dosimetric gain of prone treatments for spine lesions, and careful consideration criteria for patient selection should be applied (Fürweger et al., 2014).

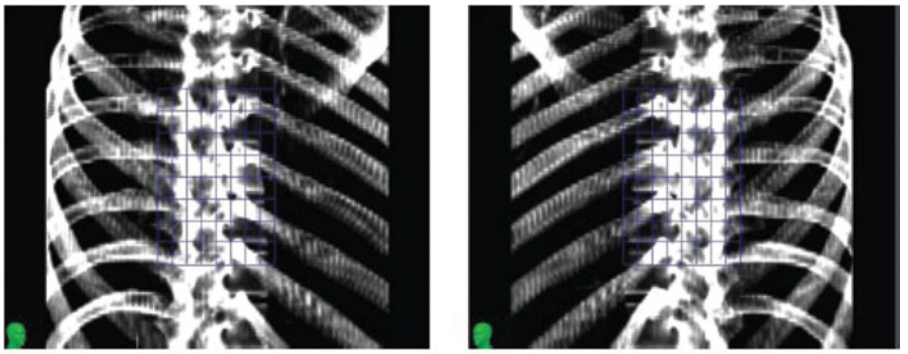

Figure 3.4 Digitally reconstructed radiographs (DRR) for the two orthogonal views are shown in panels (a) and (b). Xsight spine tracking compares features in orthogonal x-ray images taken during patient setup with DRR generated in the planning computed tomography to determine 6D corrections. The algorithm compares bony features within the blue grid shown in the figure. The user determines the grid size and location during the planning process.

3.5.5 SYNCHRONY RESPIRATORY TRACKING

Synchrony (Accuray, Inc.) is a motion management system that accounts for breathing motion. Synchrony can be used in combination with Fiducial, Xsight Lung, and Xsight Spine prone tracking. The robot position is continuously readjusted to follow a moving target based on the correlation model prediction of the target location. Prior to treatment, a series of x-ray images are used to develop a correlation model between the positions of a set of infrared light-emitting diodes (LEDs) on the patient's body surface and the target. The model is updated during treatment everytime x-ray images are taken, approximately every 60 seconds. As the patient breathes, the beams are adjusted to follow the motion. Overall tracking accuracy of less than 1.5 mm is possible using this tracking method (Sonja et al., 2011). Yang et. al. measured the 95% tracking confidence interval to be within 0.66 mm for sinusoidal respiratory motion of amplitude ≤20 mm (Yang et al., 2019).

CHECKLIST: KEY POINTS FOR CLINICAL PRACTICE

- CyberKnife enables accurate delivery of IG-HSRT treatment to patients with intracranial and spinal lesions
- The system consists of a compact linac attached to a robotic manipulator
- CyberKnife IG-HSRT is frameless as image guidance is performed constantly throughout the treatment
- Plans consist of hundreds of highly focused, noncoplanar radiation beams, which enable one to achieve highly conformal dose distribution with steep-dose gradient
- An understanding of the system operating principles is essential to plan simulation and delivery procedures appropriately

REFERENCES

Accuray Inc. (2018) CyberKnife treatment delivery system technical specifications.www.accuray.com/wp-content/uploads/cyberknife-treatment-delivery-system_-technical-specifications.pdf

Adler JR, Jr., Murphy MJ, Chang SD, Hancock SL (1999) Image-guided robotic radiosurgery. *Neurosurgery* 44(6):1299–1306.

Chuang C, Sahgal A, Lee L, Larson D, Huang K, Petti P, Verhey L, Ma L (2007) Effects of residual target motion for image-tracked spine radiosurgery. *Medical Physics* 34(11):4484.

Cox BW, Spratt DE, Lovelock M, Bilsky MH, Lis E, Ryu S, Sheehan J et al. (2012) International spine radiosurgery consortium consensus guidelines for target volume definition in spinal stereotactic radiosurgery. *International Journal of Radiation Oncology, Biology, Physics* 83(5):e597–605.

Descovich M, Ma L, Chuang CF, Larson DA, Barani IJ (2012) Comparison between prone and supine patient setup for spine stereotactic body radiosurgery. *Technol Cancer Research & Treatment* 11(3):229–236. www.ncbi.nlm.nih.gov/pubmed/22468994.

Echner GG, Kilby W, Lee M, Earnst E, Sayeh S, Schlaefer A, Rhein B et al. (2009) The design, physical properties and clinical utility of an iris collimator for robotic radiosurgery. *Physics Medical & Biology* 54(18):5359–5380.

Fu D, Kuduvalli G (2008) A fast, accurate, and automatic 2D–3D image registration for image-guided cranial radiosurgery. *Medical Physics* 35(5):2180.

Fu D, Kuduvalli G, Maurer CR, Adler JR (2006) 3D target localization using 2D local displacements of skeletal structures in orthogonal x-ray images for image-guided spinal radiosurgery. *International Journal of Computer Assist Radiological Surgery* 1:198–200.

Fürweger C, Drexler C, Kufeld M, Muacevic A, Wowra B, Schlaefer A (2010) Patient motion and targeting accuracy in robotic spinal radiosurgery: 260 single-fraction fiducial-free cases. *International Journal of Computer Assist Radiological Surgery* 78(3):937–945.

Füerweger C, Drexler C, Kufeld M, Wowra B (2011) Feasibility of fiducial-free prone-position treatments with CyberKnife for lower lumbosacral spine lesions. *Cureus* 3(1):e21.

Fürweger C, Drexler C, Muacevic A, Wowra B, de Klerck EC, Hoogeman MS (2014) CyberKnife robotic spinal radiosurgery in prone position: Dosimetric advantage due to posterior radiation access? *Journal of Applied Clinical Medical Physics/American College of Medical Physics* 15(4): 4427.

Ho AK, Fu D, Cotrutz C, Hancock SL, Chang ST, Gibbs IC, Maurer CR, Adler JR (2007) A study of the accuracy of CyberKnife spinal radiosurgery using skeletal structure tracking. *Neurosurgery* 60(2 Suppl 1):ONS147–ONS156.

Kilby W, Dooley JR, Kuduvalli G, Sayeh S, Maurer CR (2010) The CyberKnife robotic radiosurgery system in 2010. *Technology in Cancer Research & Treatment* 9(5):433–452.

Kim N, Lee H, Kim JS, Baek JG, Lee CG, Chang SK, Koom WS (2017). Clinical outcomes of multileaf collimator-based CyberKnife for spine stereotactic body radiation therapy. *The British Journal of Radiology*, 90(1079), 20170523.

Ma C-M, Li J S, Deng J, Fan J (2008) Implementation of Monte Carlo dose calculation for CyberKnife treatment planning. *Journal of Physics: Conference Series* 102:012016.

Ma L, Petti P, Wang B, Descovich M, Chuang C, Barani IJ, Kunwar S, Shrieve DC, Sahgal A, Larson DA (2011a) Apparatus dependence of normal brain tissue dose in stereotactic radiosurgery for multiple brain metastases. *Journal of Neurosurgery* 114(6):1580–1584.

Ma L, Sahfal A, Hwang A, Hu W, Descovich M, Chuang C, Barani I, Sneed PK, McDermott M, Larson DA (2011b) A two-step optimization method for improving multiple brain lesion treatments with robotic radiosurgery. *Technology in Cancer Research & Treatment* 10(4):331–338.

Maurer CR, Jr., West JB (2006) Medical image registration using mutual information. In: Heilbrun MP (ed.), *CyberKnife Radiosurgery*: *Practical Guide*, 2nd ed. Sunnyvale, CA: The CyberKnife Society.

McGuinness C, Gottschalk AR, Lessard E, Nakamura J, Pinnaduwage D, Pouliot J, Sims C, Descovich M (2015) Investigating the clinical advantages of a robotic linac equipped with a multi-leaf collimator in the treatment of brain and prostate cancer patients. *Journal of Applied Clinical Medical Physics* 16(5). doi:10.1120/jacmp.v16i5.5502.

Murphy MJ (2009) Intrafraction geometric uncertainties in frameless image-guided radiosurgery. *International Journal of Radiation Oncology, Biology, Physics* 73(5):1364–1368.

Pantelis E, Moutsatsos A, Antypas C, Zoros E, Pantelakos P, Lekas L, Romanelli P, Zourari K, Hourdakis CJ (2018) On the total system error of a robotic radiosurgery system: Phantom measurements, clinical evaluation and long-term analysis. *Physics Medical Biology* 20;63(16):165015.

Pöll JJ, Hoogeman MS, Prévost JB, Nuyttens JJ, Levendag PC, Heijmen BJ (2008) Reducing monitor units for robotic radiosurgery by optimized use of multiple collimators. Medical Physics 35(6):2294–2299.

Ryu S (2011) Radiation Oncology Group. RTOG 0631 protocol information. www.rtog.org/clinicaltrials/protocoltable/studydetails.aspx?study=0631, Open to accrual date 2011.

Sahgal A, Chuang C, Larson D, Huang K, Petti P, Weinstein P, Ma L (2008) Split-volume treatment planning of multiple consecutive vertebral body metastases for CyberKnife image-guided robotic radiosurgery. *Medical Dosimetry* 33(3):175–179.

Schlaefer A, Schweikard A (2008) Stepwise multi-criteria optimization for robotic radiosurgery. *Medical Physics* 35(5):2094.

Schüler E, Lo A, Chuang CF, Soltys SG, Pollom EL, Wang L (2020). Clinical impact of the VOLO optimizer on treatment plan quality and clinical treatment efficiency for CyberKnife. *Journal of Applied Clinical Medical Physics* 21(5):38–47.